



Physics-based Morphology Analysis and Adjoint Optimization of Flexible Flapping Wings

Joseph Shang
WRIGHT STATE UNIVERSITY

08/30/2016
Final Report

DISTRIBUTION A: Distribution approved for public release.

Air Force Research Laboratory
AF Office Of Scientific Research (AFOSR)/ RTA1
Arlington, Virginia 22203
Air Force Materiel Command

REPORT DOCUMENTATION PAGE				<i>Form Approved</i> OMB No. 0704-0188	
<p>The public reporting burden for this collection of information is estimated to average 1 hour per response, including the time for reviewing instructions, searching existing data sources, gathering and maintaining the data needed, and completing and reviewing the collection of information. Send comments regarding this burden estimate or any other aspect of this collection of information, including suggestions for reducing the burden, to the Department of Defense, Executive Service Directorate (0704-0188). Respondents should be aware that notwithstanding any other provision of law, no person shall be subject to any penalty for failing to comply with a collection of information if it does not display a currently valid OMB control number.</p> <p>PLEASE DO NOT RETURN YOUR FORM TO THE ABOVE ORGANIZATION.</p>					
1. REPORT DATE (DD-MM-YYYY) 26-08-2016		2. REPORT TYPE Final		3. DATES COVERED (From - To) June 2012- May 2016	
4. TITLE AND SUBTITLE Physics-Based Morphology Analysis and Adjoint Optimization of Flexible Flapping Wing				5a. CONTRACT NUMBER	
				5b. GRANT NUMBER FA9550-12-1-0071	
				5c. PROGRAM ELEMENT NUMBER	
6. AUTHOR(S) Dong, Haibo Wei, Mingjun				5d. PROJECT NUMBER	
				5e. TASK NUMBER	
				5f. WORK UNIT NUMBER	
7. PERFORMING ORGANIZATION NAME(S) AND ADDRESS(ES) University of Virginia Charlottesville, VA, 22904 New Mexico State University 1780 E University Ave, Las Cruces, NM 88003				8. PERFORMING ORGANIZATION REPORT NUMBER	
9. SPONSORING/MONITORING AGENCY NAME(S) AND ADDRESS(ES) Air Force Office of Scientific Research 875 N. Randolph, Ste.325 Arlington Virginia, 22203				10. SPONSOR/MONITOR'S ACRONYM(S) AFOSR	
				11. SPONSOR/MONITOR'S REPORT NUMBER(S)	
12. DISTRIBUTION/AVAILABILITY STATEMENT DISTRIBUTION A					
13. SUPPLEMENTARY NOTES					
14. ABSTRACT Changes in the dynamic morphology of the wing in flapping flights directly affect the instantaneous aerodynamic forces and therefore flight behavior. The wing shape and how it moves through the flow is the primary mechanism for momentum transfer to the fluid in the flapping flights. During this project period, high-fidelity CFD simulation and adjoint analysis/optimization tool has been used to study the aerodynamic role of wing morphology models built from the previous year and their interaction in a vast parametric space including aspect ratio, direction of flexibility (chord-wise, span-wise, etc.). Aerodynamic performance has been evaluated by looking at lift production, power consumption, and efficiency. Novel tools for studying wing morphing during complicated flapping flights have been developed to understand the underlying physics of flexible wings in flying insects and birds towards the bio-inspired wing designs with superior aerodynamic performance.					
15. SUBJECT TERMS Flapping flight, wing morphing, computational fluid dynamics (CFD), singular value decomposition (SVD), adjoint optimization					
16. SECURITY CLASSIFICATION OF:			17. LIMITATION OF ABSTRACT	18. NUMBER OF PAGES 62	19a. NAME OF RESPONSIBLE PERSON Haibo Dong
a. REPORT	b. ABSTRACT	c. THIS PAGE			19b. TELEPHONE NUMBER (Include area code) 434-243-4098

INSTRUCTIONS FOR COMPLETING SF 298

1. REPORT DATE. Full publication date, including day, month, if available. Must cite at least the year and be Year 2000 compliant, e.g. 30-06-1998; xx-06-1998; xx-xx-1998.

2. REPORT TYPE. State the type of report, such as final, technical, interim, memorandum, master's thesis, progress, quarterly, research, special, group study, etc.

3. DATES COVERED. Indicate the time during which the work was performed and the report was written, e.g., Jun 1997 - Jun 1998; 1-10 Jun 1996; May - Nov 1998; Nov 1998.

4. TITLE. Enter title and subtitle with volume number and part number, if applicable. On classified documents, enter the title classification in parentheses.

5a. CONTRACT NUMBER. Enter all contract numbers as they appear in the report, e.g. F33615-86-C-5169.

5b. GRANT NUMBER. Enter all grant numbers as they appear in the report, e.g. AFOSR-82-1234.

5c. PROGRAM ELEMENT NUMBER. Enter all program element numbers as they appear in the report, e.g. 61101A.

5d. PROJECT NUMBER. Enter all project numbers as they appear in the report, e.g. 1F665702D1257; ILIR.

5e. TASK NUMBER. Enter all task numbers as they appear in the report, e.g. 05; RF0330201; T4112.

5f. WORK UNIT NUMBER. Enter all work unit numbers as they appear in the report, e.g. 001; AFAPL30480105.

6. AUTHOR(S). Enter name(s) of person(s) responsible for writing the report, performing the research, or credited with the content of the report. The form of entry is the last name, first name, middle initial, and additional qualifiers separated by commas, e.g. Smith, Richard, J, Jr.

7. PERFORMING ORGANIZATION NAME(S) AND ADDRESS(ES). Self-explanatory.

8. PERFORMING ORGANIZATION REPORT NUMBER. Enter all unique alphanumeric report numbers assigned by the performing organization, e.g. BRL-1234; AFWL-TR-85-4017-Vol-21-PT-2.

9. SPONSORING/MONITORING AGENCY NAME(S) AND ADDRESS(ES). Enter the name and address of the organization(s) financially responsible for and monitoring the work.

10. SPONSOR/MONITOR'S ACRONYM(S). Enter, if available, e.g. BRL, ARDEC, NADC.

11. SPONSOR/MONITOR'S REPORT NUMBER(S). Enter report number as assigned by the sponsoring/monitoring agency, if available, e.g. BRL-TR-829; -215.

12. DISTRIBUTION/AVAILABILITY STATEMENT. Use agency-mandated availability statements to indicate the public availability or distribution limitations of the report. If additional limitations/ restrictions or special markings are indicated, follow agency authorization procedures, e.g. RD/FRD, PROPIN, ITAR, etc. Include copyright information.

13. SUPPLEMENTARY NOTES. Enter information not included elsewhere such as: prepared in cooperation with; translation of; report supersedes; old edition number, etc.

14. ABSTRACT. A brief (approximately 200 words) factual summary of the most significant information.

15. SUBJECT TERMS. Key words or phrases identifying major concepts in the report.

16. SECURITY CLASSIFICATION. Enter security classification in accordance with security classification regulations, e.g. U, C, S, etc. If this form contains classified information, stamp classification level on the top and bottom of this page.

17. LIMITATION OF ABSTRACT. This block must be completed to assign a distribution limitation to the abstract. Enter UU (Unclassified Unlimited) or SAR (Same as Report). An entry in this block is necessary if the abstract is to be limited.

Physics-based Morphology Analysis and Adjoint Optimization of Flexible Flapping Wings

Grant number: AFOSR FA95500-12-1-0071

Principal Investigator (PI): Haibo Dong, University of Virginia

Co-PI: Mingjun Wei, New Mexico State University

Program Officer: Douglas R. Smith

Contents

List of Figures	iii
1. Proposed Research and Technical Objectives	7
2. Physics-based Morphology Analysis	7
2.1 Joint-based 3D Surface Reconstruction	9
2.2 High-fidelity Numerical Simulations on the Aerodynamics of Morphing Wings	11
2.3 Low-dimensional Modeling and Analysis of the Morphing Wing Kinematics	31
2.4 Optimization of Low-dimensional Morphing Wing Models	40
3. Adjoint Optimization	43
3.1 Governing equations for adjoint optimization	44
3.2 Numerical algorithm	46
3.3 Validation of adjoint-based optimization solution and gradient information	47
3.4 Applications to optimize the kinematics and deformation of flapping wings	49
4. References	56

List of Figures

Figure 1. (a) Static model of dolphin with virtual joints; (b) virtual joints configuration based on real hummingbird skeletal anatomy.....	10
Figure 2. Raw pictures of real hummingbird and its reconstructed model at (a, d) $t=0$ ms, (b, e) $t=47$ ms, and (c, f) $t=77$ ms.	11
Figure 3. Schematic describing the naming convention and location of velocity components employed in the spatial discretization of the governing equations.....	12
Figure 4. (a) Example of a hummingbird model with unstructured surface mesh of triangular elements; (b) 2D schematic describing the methodology which handles deformable attaching bodies.	13
Figure 5. (a) Schematic plot showing hummingbird body yaw motion; (b) time course of body of the maneuvering hummingbird. A top view of the hummingbird at the top of the figure indicates the yaw throughout the maneuver. Yaw (red), pitch (black), and roll (blue) histories are shown first, followed by path position histories in horizontal (green) and vertical (black) direction.	15
Figure 6. (a) Schematic plot showing hummingbird wing Euler angles definition; Time course of wing stroke (b), wing deviation (c), and wing pitch angles (d) during the turning phase. The wing Euler angle histories over the 3rd stroke are shown in solid curves. Angle differences for other strokes in the turning phase with respect to the 3rd stroke are shown as error bars. Red and blue correspond to the inner and outer wings, respectively. Shaded areas stand the downstrokes and unshaded areas stand the upstrokes.	16
Figure 7. Schematic of the computational mesh and boundary conditions employed in the current simulation.	Error! Bookmark not defined.
Figure 8. Time course of lift (a) and drag (b) coefficients during the turning phase of hummingbird pure yaw turn. The force coefficient histories over the 3rd stroke are shown in solid curves. Force coefficient differences for other strokes in the turning phase with respect to the 3rd stroke are shown as error bars. Red and blue correspond to the inner and outer wings, respectively. Shaded areas stand the downstrokes and unshaded areas stand the upstrokes.	17
Figure 9. (a-f) Time course of vortex development of the 3rd stroke of the hummingbird pure yaw turn, visualized by the Q-criterion. The vortex structures are colored by non-dimensional pressure.....	19
Figure 10. (a) Isosurface of pressure corresponding to a non-dimensional value of -1.0 at $t/T=0.37$ of the 3rd stroke of the hummingbird pure yaw turn; (b) wake schematic at $t/T=0.37$ of the 3rd stroke of the hummingbird pure yaw turn.	Error! Bookmark not defined.
Figure 11. Real cicada and its reconstruction. (a) Raw picture; (b) Comparison of real and reconstructed cicada.	20
Figure 12. Stoke angle (0° lateral, downstroke positive), deviation angle (upward positive), and pitch angle (rotation around wing span, smaller than 90° when leading edge is forward) for the forewing (a) and the hindwing (b).	21

Figure 13. Time course of vortices development, visualized by Q-criterion. The left and middle columns are back view and top view respectively, and the vortex structures are coloured by spanwise vorticity. The right column shows the structures in projection view, coloured by streamwise vorticity. Color bars in the first row apply to figures in the same column.....	23
Figure 14. Transverse plane cut at mid-downstroke. (a) Cut through wing and body (b) Cut through the near wake (no wings or body being cut). Contour of Q-criterion, velocity vector, and two-dimensional streamline seen from the back view.	23
Figure 15. Time traces of lift and thrust coefficients of the body (a) and a single wing (b) during the fourth flapping cycle when both the aerodynamic forces and flow reach a periodic state. Peak 1 and 2 in figure (a) occur at $t/T=0.3$ and 0.74 , respectively.....	24
Figure 16. Surface pressure coefficient distribution on the body for the WB model at selected instants: (a) $t/T=0.3$; (b) $t/T=0.74$; (c) $t/T=0.9$	25
Figure 17. Pressure difference between the upper and lower wing surface (ΔC_p) of the right wing for the WB model (a) and WN model (b), respectively. (c) Shows the difference ΔC_p of between (a) and (b).....	25
Figure 18. Isosurface of pressure coefficient ($C_p = -0.2$) at $t/T=0.3$ for (a) the WN model and (b) the WB model. Wake schematic for (c) the WN model and (d) the WB model at $t/T=0.3$	26
Figure 19. (a) Chord-lines of dragonfly forewing (dashed line) and hindwing (solid line) at a few instances. (b) Definition of wing orientation angles, wing stroke angle (ψ), wing deviation angle (ϕ), wing pitch angle (θ), and camber deformation (h/c). (c-e) Time course of wing kinematics of dragonfly hindwing. (c) Wing stroke angle (ψ) and wing deviation angle (ϕ). (d) and (e) are the wing pitch angles (θ) and camber deromation (h/c) of different sections along the wing span, respectively. The downstroke period is shaded as a gray color.	28
Figure 20. Time course of lift (a), thrust (b) and power (c) of the hindwing.	29
Figure 21. Comparison of vortex formation along the wing span at the mid-downstroke ($t/T=0.31$). (a) Original wing. (b) Twist-only wing (c) Rigid wing. The vortical structure including leading-edge vortex (LEV), trailing-edge vortex (TEV), and secondary vortex (SV) are labeled.	Error! Bookmark not defined.
Figure 22. Motion reconstruction of dragonfly taking-off maneuver. The side panels show 4 of 110 frames recorded by high-speed videography.	30
Figure 23. 3-D vortex structures in the flow during the early turning motion, where the time stamp from (a) to (d) is 23, 29, 35 and 40 ms. The vortex loop from the downstroke is marked by dashed lines.	31
Figure 24. The SSVD spectrum of the first ten modes for the dragonfly right forewing kinematics. The left ordinate shows $ \lambda_i /\sum \lambda_i $, and the right ordinate shows the cumulative value of the left ordinate.	34
Figure 25. Wing motions of (a) experimental kinematics (also called the mode-all case), (b) SSVD mode 1, (c) mode 2 and (d) low-dimensional model mode 1+2. The wings are colored with distances between wing surfaces and corresponding least square planes. The distances are normalized by wing mid chord length.....	34

Figure 26. Comparison of the time variation of aerodynamic performances between the mode-all and low-dimensional gaits. (a) lift; (b) drag; (c) power.....	36
Figure 27. 2D slices of the leading edge vortex along the wingspan (10%~90%) at two time instances for (a, b) mode-all, (c, d) mode 1, and (e, f) mode 1+2 cases. The corresponding vortex center are marked with green dots at each slice. The contours represent normalized span-wise vorticity.	37
Figure 28. Distances of LEV center to the wing surface (lift-off distances) at (a) $t/T=0.25$ and (b) $t/T=0.75$ for mode-all, mode 1, and mode 1+2 cases.	38
Figure 29. LEV circulations at (a) $t/T=0.25$ and (b) $t/T=0.75$ for mode-all, mode 1, and mode 1+2 cases.	39
Figure 30. Convergence history for design variables (a) W_1 , (b) W_2 , and (c) φ of the two optimization cases.	40
Figure 31. Comparison of the time course of aerodynamic performance of Mode 1+2 and optimized wing gaits. (a) Lift; (b) power.	41
Figure 32. Time averaged lift and power coefficients projected on the wing surface for the cases (a, b) Mode 1+2, (c, d) Opt C_L , and (e, f) Opt η ... Error! Bookmark not defined.	
Figure 33. Wake structures for the (a) Mode 1+2, (c) Opt C_L , (e) Opt η at $t/T=0.27$; wake structures for the (b) Mode 1+2, (d) Opt C_L , (f) Opt η at $t/T=0.73$	42
Figure 34. A typical snapshot showing the plunging plate, the flow and the observation region.	
Figure 35. Adjoint-based optimization for the plunging velocity: (a) change of the cost function J and the gradient norm $ g $ with the number of iterations; (b) comparison of the initial control ϕ_1 (---), the target control ϕ_0 (— . —) and the optimal control ϕ_p (—)).	
Figure 36. Comparison of the gradient g between the values computed by the adjoint method (line) and the finite difference approach through direct perturbation (square).	
Figure 37. Adjoint-based optimization for the plunging velocity with a different initial control.49	
Figure 38. Optimization for the drag reduction of a rigid flapping plate: (a) the cost function for drag reduction versus the number of iterations; (b) the optimal constant control (---) and the optimal time-varying control (—), with dash-dot lines representing the constraints.	
Figure 39. The vortex structures of a flapping plate with (a) the initial time constant, (b) optimal the time-constant and (c) the optimal time-varying phase delay during the upstroke.	
Figure 40. The history of drag forces in one period for case 1 (—), case 2 (---), case 3 (— . —) and case 4 (.....) of Group I.	
Figure 41. Comparison of kinematics, deformation and vortex structures of (a) the rigid plate (case 1), (b) the plate with small deformation (case 2), (c) the plate with large deformation (case 3) and (d) the reference (case 4), with $Re=300$ (Group I), at $t=0, 1$ and 1.5 .	
Figure 42. The time history of the lift coefficients for a rigid hovering plate with the initial control (---) and the optimal control (—).	
Figure 43. The z-component of vorticity at the middle plane for a rigid hovering plate with (a) the initial control and (b) the optimal control at different time moments.	

Figure 44. The pressure distribution of a rigid hovering plate with (a) the initial control and (b) the optimized control on the lower (left) and upper (right) surfaces at different time moments.

Figure 45. The vortex structures of a rigid hovering plate with (a) the initial control and (b) the optimal control at different time moments.

Project name: Physics-Based Morphology Analysis and Adjoint Optimization of Flexible Flapping Wing

Grant number: AFOSR FA95500-12-1-0071

Principal Investigator (PI): Haibo Dong, University of Virginia

Co-PI: Mingjun Wei, New Mexico State University

1 Proposed Research and Technical Objectives

Changes in the dynamic morphology of the wing in flapping flights directly affect the instantaneous aerodynamic forces and therefore flight behavior. The wing shape and how it moves through the flow is the primary mechanism for momentum transfer to the fluid in the flapping flights. During this project period, high-fidelity CFD simulation and adjoint analysis/optimization tool has been used to study the aerodynamic role of wing morphology models built from the previous year and their interaction in a vast parametric space including aspect ratio, direction of flexibility (chord-wise, span-wise, etc.). Aerodynamic performance has been evaluated by looking at lift production, power consumption, and efficiency. Novel tools for studying wing morphing during complicated flapping flights have been developed to understand the underlying physics of flexible wings in flying insects and birds towards the bio-inspired wing designs with superior aerodynamic performance. In this funded work, we built up a team with experts from two institutes and hope to address the following basic questions about the aerodynamics of flapping flight:

1. What are the detailed features of morphing flapping wings and how to build up high-fidelity kinematic models?
 2. What is the proper way(s) to characterize the wing morphing and describe the key motion components?
 3. What is the vortex dynamics and associated aerodynamics in morphing wing flapping flight?
 4. How to design morphing wing kinematics to achieve the optimal performance of the wing beyond biology?
 5. What is optimal solution for 2D and 3D rigid/flexible flapping wings, and what we can learn from these mathematically optimal solutions?
-

2 Physics-based Morphology Analysis

In this part, four sections regarding the physics-based morphology analysis on the proposed topic are presented. We briefly summarize these works in the following.

- (1) Joint-based morphing surface reconstruction

- A high-accurate kinematics measurement tool is developed to quantify the propulsor flexion and body kinematics of animals in free flight.
- (2) High-fidelity Numerical Simulations on the Aerodynamics of Morphing wings
- An immersed boundary method for deformable attaching bodies (IBM-DAB) is developed to handle direct numerical simulations in some extreme situations that are commonly exist in nature, including solid bodies with sharp edges and those with deformable, attaching membrane bodies.
 - The 3D wake structures and aerodynamic performance of a freely maneuvering hummingbird is studied in detail. Our simulation results show asymmetric wake structure between inner and outer wings of the hummingbird. A unique duel-ring vortex structure, which is the source of the wake asymmetry, is found in the wake of one of the two wings of the hummingbird. The duel-ring vortex structure corresponds to larger wing twisting and lower drag production, which creates unbalanced aerodynamic forces to help with the maneuver
 - Free forward flight of cicadas has been investigated through high speed photogrammetry, three-dimensional surface reconstruction and computational fluid dynamics simulations. We report two new vortices generated by the cicada body. One is the thorax generated vortex, which helps the downwash flow, indicating a new phenomenon of lift enhancement. Another is the cicada posterior body vortex, which entangles with the vortex ring composed of wing tip, trailing edge, and wing root vortices.
 - A new lift-enhancement mechanism due to the wing-body interaction has been found in cicada forward flight. Our results have shown that due to wing-body interaction, the wing-body model of the cicada flight had a 18.7% increase in total lift production compared with the sum of the lift generated in body-only and wings-only models, and about 65% of this enhancement was attributed to the body. This resulted from a dramatic improvement of body lift production from 2% to 11.6% of the total lift produced by the wing-body system. Further analysis of the associated near-field and far-field vortex structures has shown that this lift enhancement was attributed to the formation of two distinct vortices shed from the thorax and the posterior of the insect, respectively, and their interactions with the flapping wings.
 - Aerodynamic effects of the wing morphing in dragonfly forward flight is computationally investigated. We use the reconstructed model to explore the effects of morphing wings, first by removing camber while keeping the same time-varying twist distribution, and second by removing both the camber and the spanwise twist. Our simulation results revealed that the surface deformation can improve the aerodynamic functions in two ways: 1) improving the power economy by preventing the tip vortex bursting; and 2) improving the leading-edge vortex attachment by suppressing the generation of the secondary vortex. As a result, the spanwise twist can boost the aerodynamic efficiency up to 20%, especially during the wing translational phase.
 - Aerodynamic functions and associated vortex formation of the two-pair wings of a dragonfly in turning maneuver is numerically investigated. The wing kinematics analysis indicate that during the turn there are large asymmetries between the wing pitch angle and wing stroke angles especially for forewings, while asymmetries in wing deviation angle are generally small. The asymmetrical wing kinematics generate unbalanced forces in both vertical and horizontal directions. During the downstroke, the force generated by the outer wings are higher than inner wings. By contrast, the inner wings generate higher

forces during the upstroke. The unbalanced forces lead to the torques along its body axis in three directions. Specifically, both forewings and hindwing contribute to the roll torque generation, whereas forewings are dominant in generating pitch and yaw torques. To examine the effect of forewing-hindwing interaction on the aerodynamic performance, two additional cases, one with forewings only and the other with hindwings only, are carried out. Our results indicate that the interaction can lead to a slight forces reduction, but can save the aerodynamic power up to 11%.

(3) Low-dimensional Modeling (SVD) and Analysis of the Morphing wing kinematics

- The aerodynamic roles of wing morphing of a hovering dragonfly is studied in detail. A spherical-coordinates-based singular value decomposition (SSVD) method is developed and applied to decompose the morphing wing kinematics of the dragonfly into simple modes. Results have shown that the first two SSVD modes contain 93.1% of the hovering wing motion. The mode 1 (flapping mode) consists of a simple flapping motion, and the mode 2 (morphing mode) contains dynamic wing morphing in both span-wise and chord-wise directions. By evaluating the aerodynamic role of the SSVD modes using a high-fidelity flow simulation, we further conclude that the first two modes can recover more than 96% of the lift production and 91% of the lift economy comparing to the original flapping wing aerodynamics whereas the mode 1 only produces 5% of the lift and 4% of the lift economy. The associated flow mechanisms of the morphing mode are found to be the reduced wing tip vortex and improved attachment of leading-edge vortex

(4) Optimization of low-dimensional morphing wing models

- We further investigated optimal configurations of dominant modes on aerodynamic performance for the dragonfly wing. The corresponding optimized low dimensional wing models, which can beyond biological levels of aerodynamic performance, are obtained. The associated flow mechanisms are found to be the improved LEV strength and the reduced TV strength.

2.1 Joint-based 3D Surface Reconstruction

Recently, advanced photogrammetry technology has been used to study flapping wings in nature. Along with the highly accurate surface reconstruction method [1], researchers are capable of digitizing detailed propulsor kinematics, as well as deformation from high-speed images. However, the conventional reconstruction method has several hard constraints regarding some details of the experiments, such as the camera location/orientation, the lens angle of view, marker points on the objects, etc. For example, it is usually difficult for us to configure three orthogonal high-speed cameras to conduct experiments. For some fast and agile flyers, such as hummingbird, it is not possible for us to use lenses with a small angle of view due to their large movements. Perspective error becomes a big issue in those cases. Moreover, placing marker points on the wings could be hard due to the wings' size or properties. A more robust reconstruction method is needed to deal with diverse flapping wings in nature.

A joint-based surface reconstruction method is developed in Autodesk Maya to solve the above problems in this work. Here we use a case of a maneuvering hummingbird to demonstrate the new method.

1) Static Model and Virtual Joints

In order to perform the reconstruction, a realistic static model of the hummingbird with some carefully configured motion controllers, which are so called “virtual joints”, is needed at first.

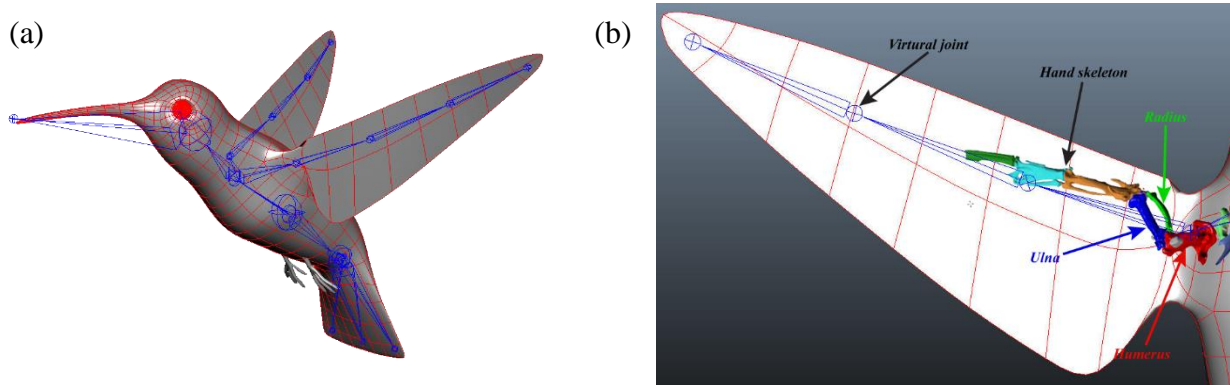


Figure 1. (a) Static model of hummingbird with virtual joints; (b) virtual joints configuration based on real hummingbird skeletal anatomy.

Figure 1(a) shows the static model of the hummingbird with virtual joints, which is manually created with Autodesk Maya. The dimensions of the model strictly match with the real hummingbird we are going to study. The virtual joints have six degrees of freedoms (three translations and three rotations) to control the motion of adjacent vertices of the model. Figure 1(b) shows the virtual joints configuration at the hummingbird wing, which presents large deformation during the flapping motion. This kind of configuration can model both the span and chordwise morphing of the wing. As shown in the figure, the virtual joints are built based on a real hummingbird’s skeletal anatomy. However, some parts of the wing, which presents large motion in flight, do not really have bone structures, such as the wing tip region. We also add virtual joints to control the motion for those parts.

2) Wing and Body Surface Reconstruction

The hummingbird maneuvering flight is then reconstructed using the joint-based hierarchical subdivision surface method. The hummingbird wings are marked with white marker points to facility the three-dimensional surface reconstruction. After the videotaping was done, the pose of the model is adjusted to match one frame of the three directions of high-speed videos by controlling the virtual joints in six degrees of freedom, including three rotations and three translations. Marker points on the wings served as references to further tune the location of vertices on the wing models. The wing models are generated with Catmull-Clark subdivision surfaces [2], which is a specific cubic spline surface representation that can generate smooth surfaces from meshes of arbitrary topology [3]. Similar procedure is applied to the hummingbird model frame by frame. As an example, Figure 1(a, b, and c) show the poses of the corresponding reconstructed hummingbird model.

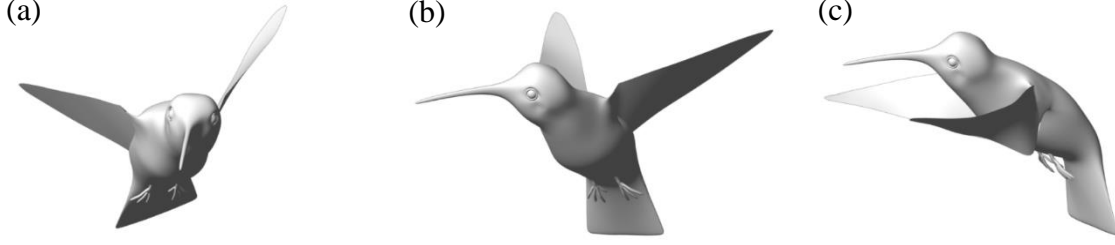


Figure 2. Reconstructed model of hummingbird maneuvering flight at (a) $t=0$ ms, (b) $t=47$ ms, and (c) $t=77$ ms.

2.2 High-fidelity Numerical Simulations on the Aerodynamics of Morphing Wings

1) Immersed Boundary Method for Deformable Attaching Bodies

The governing equations considered are the 3D unsteady Navier-Stokes equations for a viscous incompressible flow with constant properties given by:

$$\begin{cases} \frac{\partial u_i}{\partial x_i} = 0 \\ \frac{\partial u_i}{\partial t} + \frac{\partial(u_i u_j)}{\partial x_j} = -\frac{1}{\rho} \frac{\partial p}{\partial x_i} + \nu \frac{\partial}{\partial x_j} \left(\frac{\partial u_i}{\partial x_j} \right) \end{cases} \quad (1)$$

where $i, j=1, 2, 3$, u_i are the velocity components, p is the pressure, and ρ and ν are the fluid and kinematic viscosity.

The Navier-Stokes equations(1) are discretized using a cell-centered, collocated (non-staggered) arrangement of the primitive variables u_i and p . In addition to the cell-center velocities u_i , the face-center velocities U_i , are computed (see Figure 3). The equations are integrated in time using the fractional step method, which consists of three sub-steps. In the first sub-step of this method, a modified momentum equation is solved and an intermediate velocity u^* is obtained. A second-order, Adams-Bashforth scheme is employed for the convective terms while the diffusion terms are discretized using an implicit Crank-Nicolson scheme, which eliminates the viscous stability constraint. In this sub-step, the following modified momentum equation is solved at the cell-nodes:

$$\frac{u_i^* - u_i^n}{\Delta t} = \frac{1}{2} \left[3 \frac{\delta(U_j^n u_i^n)}{\delta x_j} - \frac{\delta(U_j^{n-1} u_i^{n-1})}{\delta x_j} \right] = -\frac{1}{\rho} \frac{\delta p^n}{\delta x_i} + \frac{1}{2} \nu \left[\frac{\delta}{\delta x_j} \left(\frac{\delta u_i^*}{\delta x_j} \right) + \frac{\delta}{\delta x_j} \left(\frac{\delta u_i^n}{\delta x_j} \right) \right] \quad (2)$$

where $\frac{\delta}{\delta x}$ corresponds to a second-order central difference. This equation is solved using a line-SOR scheme [4].

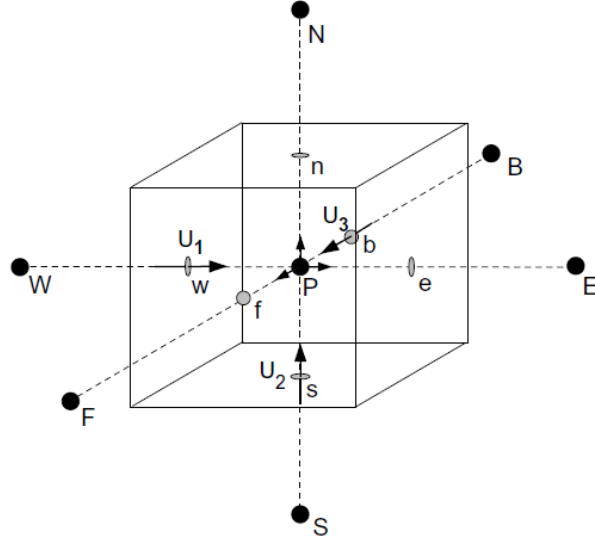


Figure 3. Schematic describing the naming convention and location of velocity components employed in the spatial discretization of the governing equations.

The second sub-step requires the solution of the pressure correction equation:

$$\frac{u_i^{n+1} - u_i^*}{\Delta t} = -\frac{1}{\rho} \frac{\delta p'}{\delta x_i} \quad (3)$$

which is solved with the constraint that the final velocity u_i^{n+1} be divergence-free. This gives the following Poisson equation for the pressure correction:

$$\frac{1}{\rho} \frac{\delta}{\delta x_i} \left(\frac{\delta p'}{\delta x_i} \right) = \frac{1}{\Delta t} \frac{\delta U_i^*}{\delta x_i} \quad (4)$$

and a Neumann boundary condition imposed on the pressure correction at all boundaries.

This Poisson equation is solved with a highly efficient geometric multigrid method [5], which employs a modified strongly implicit procedure (MSIP) [6] smoother. The ability to employ such methods is another key advantage of the current Cartesian grid approach over body-conformal unstructured grid approaches. Geometrical multigrid methods are relatively simple to implement and have very limited memory overhead. Furthermore, when coupled with powerful smoothers like line-Gauss-Siedel or MSIP, they can lead to a numerical solution of the pressure Poisson equation which scales almost linearly with the number of grid points. In contrast, for unstructured body-conformal methods, one has to either resort to algebraic multigrid methods [7, 8] or other more complex methods such as agglomeration multigrid [9]. Another choice for solving the pressure Poisson equation would be Krylov subspace based methods (such as conjugate gradient or GMRES) but these require effective preconditioners to provide good performance. Our past experience with both stationary and non-stationary iterative methods [10-12] indicates that geometric multigrid methods are very well suited for sharp interface immersed boundary methods, and we have therefore used this method in the current solver.

Once the pressure correction is obtained, the pressure and velocity are updated as:

$$\begin{cases} p^{n+1} = p^n + p' \\ u_i^{n+1} = u_i^* - \Delta t \frac{1}{\rho} \left(\frac{\delta p'}{\delta x_i} \right) \end{cases} \quad (5)$$

The motions of natural animals are reconstructed using the method introduced in Section 2.1. As shown in Figure 4(a), the surface of a reconstructed model is represented as unstructured mesh with triangular elements. The trunk body of the hummingbird is modeled as “solid body”, and the wings are modeled as “membrane body”, which presents zero thickness in the simulation. The two types of bodies firmly attached with each other, and the boundary conditions near the body intersections are difficult to deal with. Here, a new approach is introduced to overcome the computational difficulties.

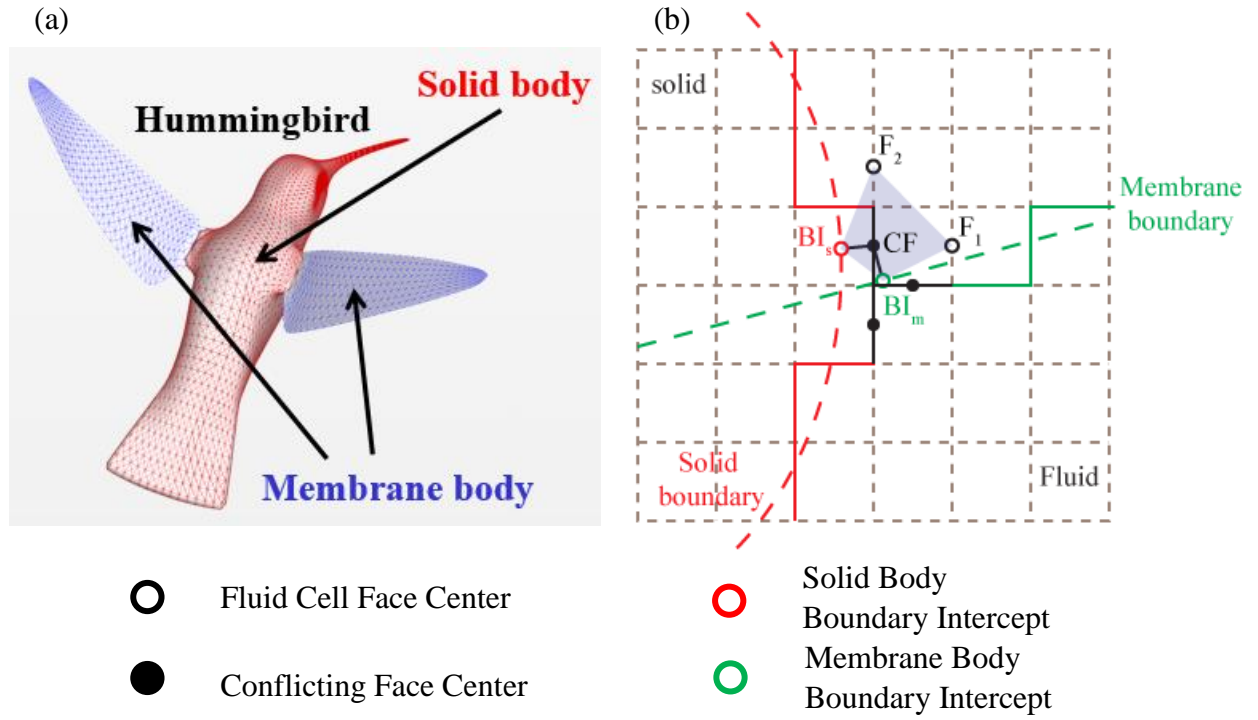


Figure 4. (a) Example of a hummingbird model with unstructured surface mesh of triangular elements; (b) 2D schematic describing the methodology which handles deformable attaching bodies.

Figure 4(b) shows a 2D schematic plot of the approach. The dashed lines are immersed boundaries and the solid lines are the corresponding stair boundaries. For the membrane body, the stair boundaries are chosen as the closest fluid cell faces to the elements on the immersed boundary. As shown in the figure, several conflicting faces can be identified. The conflicting faces are stair boundaries which directly connect to the intersection of the solid and the membrane stair boundaries. The boundary conditions on the conflicting faces need special treatments. The velocity of one conflicting face may be calculated according to a reference velocity of the solid immersed boundary at one time step. For the next time step, the reference

velocity may be altered to the velocity of the membrane immersed boundary due the motion of the moving boundaries. This will cause a discontinuity of the velocity boundary condition on the conflicting face for those two time steps, which will cause numerical instability and eventually lead to the divergence of the flow solver.

In order to solve the above problem, the velocities of the conflicting faces are corrected accordingly. Here we describe the method using the upper conflicting face (Figure 4b) as an example. From the center of the conflicting face, we first drop two lines perpendicular to the solid and membrane immersed boundaries. There we get two boundary intercept, BI_s and BI_m . Another two fluid cell faces which are close to the conflicting face can be found, and the corresponding face centers are F_1 and F_2 . An interpolation stencil (shaded area) is formed according to the four points. In 3D cases, the stencil consists of eight points (two boundary intercept and six fluid cell face centers). The conflicting face velocity can then be calculated as follows:

$$U_{CF}(x_1, x_2, x_3) = C_1 x_1 x_2 x_3 + C_2 x_1 x_2 + C_3 x_2 x_3 + C_4 x_1 x_3 + C_5 x_1 + C_6 x_2 + C_7 x_3 + C_8 + O(\Delta^2) \quad (6)$$

The eight unknown interpolation coefficients can be determined in terms of the face velocities of the eight points of the interpolation stencil:

$$\{C_1, C_2, \dots, C_8\}^T = [V]^{-1} \{U_1, U_2, \dots, U_8\}^T \quad (7)$$

where U_i are the face velocities at the interpolation stencil points and $[V]$ is the Vandermonde matrix. This process continues until the velocities of all conflicting faces are corrected.

2) Asymmetric Aerodynamic Forces and Wake Structures of a Maneuvering hummingbird

Hummingbirds perform turning maneuvers as often as they hover or cruise, especially when they need to forage from one location to another. However, to date, turning flight has received little attention and there is no detailed forces and three-dimensional flow structure data to achieve a quantitative analysis of hummingbird in a turning maneuver. To fill this gap, a high-speed photogrammetry system and three-dimensional joint-based surface reconstruction technology are used to reveal hummingbird wing kinematics and deformations during a free maneuvering flight. The aerodynamic performance is then studied using an in-house immersed boundary method (IBM) based computational fluid dynamics (CFD) solver. To the best of our knowledge, this is the first study on the unsteady aerodynamics of hummingbird in maneuvering flight.

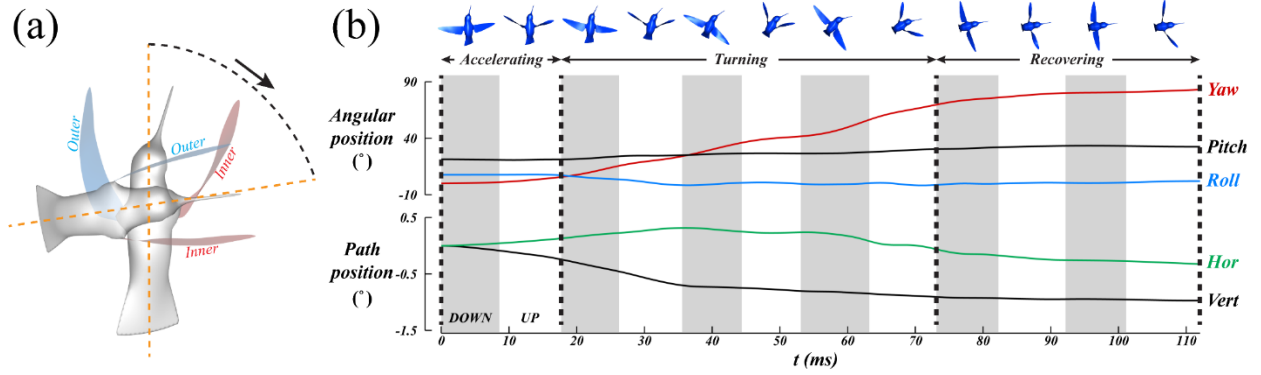


Figure 5. (a) Schematic plot showing hummingbird body yaw motion; (b) time course of body of the maneuvering hummingbird. A top view of the hummingbird at the top of the figure indicates the yaw throughout the maneuver. Yaw (red), pitch (black), and roll (blue) histories are shown first, followed by path position histories in horizontal (green) and vertical (black) direction.

To better interpret the characteristics of body and wing kinematics, we divided the whole maneuvering process into three phases according to the body yaw angle. Figure 5 shows a schematic plot of hummingbird body yaw motion and the time course of body kinematics. We can see from Figure 5(b) that there are in total six strokes of this flight. The hummingbird is first at an “accelerating phase” (1st stroke), in which the bird initiates the yaw turn. The body yaw angle start to increase while the other two Euler angles stay unchanged within this phase. After that, the hummingbird enters a “turning phase” for the following three strokes (2nd to 4th stroke). The body yaw angle keep increasing and shows an oscillating profile, which indicates an active control of the turning for the hummingbird. The body roll angle shows a little bit decrease and the body pitch angle stays unchanged. The last two strokes of the flight (5th to 6th stroke) are called the “recovering phase”, in which the body yaw angle stays at a high value and shows a small increase, while the other two Euler angles stay unchanged. The hummingbird is recovering from a turning status to a hovering status within this phase. The path position of this flight (Figure 5b) shows a little bit descending motion in vertical direction for the first two strokes, and the motion in horizontal direction is limited. We have observed similar phases in other maneuvering high-speed videos we shoot. The similarity suggests that the body motion result from similar aerodynamic or dynamic mechanisms.

In order to determine how hummingbird change wing motion to perform the turning, we also study the wing kinematics of this flight. Figure 6(a) shows the three Euler angles defining the wing position in the wing-root coordinate system ($X'Y'Z'$), in which the X' -axis is parallel with the body longitudinal direction, the Y' -axis is along the lateral direction and the Z' -axis complies with the right-hand rule. The mean stroke plane connected the wing root and wingtips at the start and end of the downstroke. The stroke position angle $\phi(t)$ defines the angular position of the wing in the mean stroke plane, with 0° aligning with the negative direction of the Y' -axis. The deviation angle $\theta(t)$ is the angle between the base-to-wingtip line and the mean stroke plane. The pitch angle $\alpha(t)$ is defined as the angle of the wing chord with respect to the tangent of the wing trajectory.

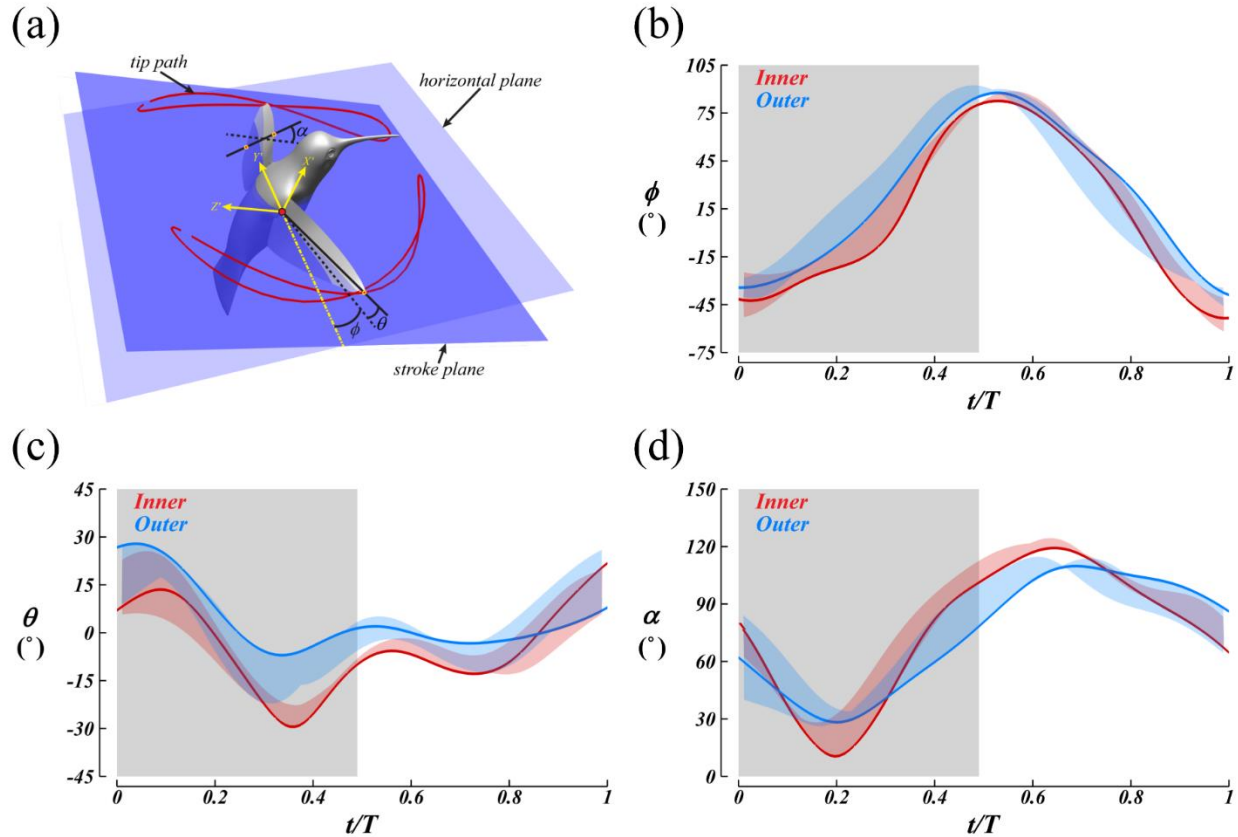


Figure 6. (a) Schematic plot showing hummingbird wing Euler angles definition; Time course of wing stroke (b), wing deviation (c), and wing pitch angles (d) during the turning phase. The wing Euler angle histories over the 3rd stroke are shown in solid curves. Angle differences for other strokes in the turning phase with respect to the 3rd stroke are shown as error bars. Red and blue correspond to the inner and outer wings, respectively. Shaded areas stand the downstrokes and unshaded areas stand the upstrokes.

The time course of wing Euler angles during the turning phase are shown in Figure 6(b, c, d) according to the above definitions. We can see from the figure that asymmetries of the wing kinematics between inner and outer wings can be identified in the turning phase, especially for the time course of wing deviation angle and pitch angle. As shown in Figure 6(b), the wing stroke angle history shows one peak for a flapping cycle, which locates at the end of the downstroke. The amplitude of the wing stroke angle is around 120° for both inner and outer wings. However, the inner wing stroke angle is a little bit smaller (7% smaller) during the downstroke in turning phase, while it is almost the same comparing to that during the upstroke. For the wing deviation angle history, the plot shows two valleys for a flapping cycle, which is located near the mid of downstroke and the mid of upstroke, respectively. Much greater differences can be observed for the wing deviation angle history. The inner wing deviation angle history shows larger amplitude and smaller value in both downstroke and upstroke. This is because of the outer wing stroke plane of the hummingbird is tilted up in the turning phase, and also, the figure eight motion of the outer wing is smaller comparing to that of the inner wing. For the wing pitching angle histories, all plots show one valley and one peak near the mid downstroke and mid upstroke, respectively. More importantly, the wing pitching angle histories

show great asymmetry between the inner and outer wings in the turning phase. The valley value of the inner wing pitching angle is much smaller than that of the outer wing, while the peak value is much greater. It leads to the average angles of attack during both the downstroke and the upstroke being much smaller for the inner wing.

CFD simulation is conducted using the kinematics of the wings and the body from the three-dimensional surface reconstruction. The time course of the averaged aerodynamic forces produced in the turning phase (average over the 2nd~4th stroke) are shown in Figure 7(a, b). We can see from Figure 7(a) that the lift coefficients for both inner wing and outer wing show two peaks in one complete stroke. The peaks locate at around 50% of each half stroke, and it is worth noting that the average values of the lift coefficient in downstroke are much higher than that in upstroke. This conforms to the previous conclusion made on a hovering hummingbird by Song et al. [13]. However, the double peaks in upstrokes, which are also reported by this paper, are not observed in this maneuvering case. A possible explanation for that is, due to the body motion of the maneuvering hummingbird, the effects of wake capture during the stroke reversal is weakened.

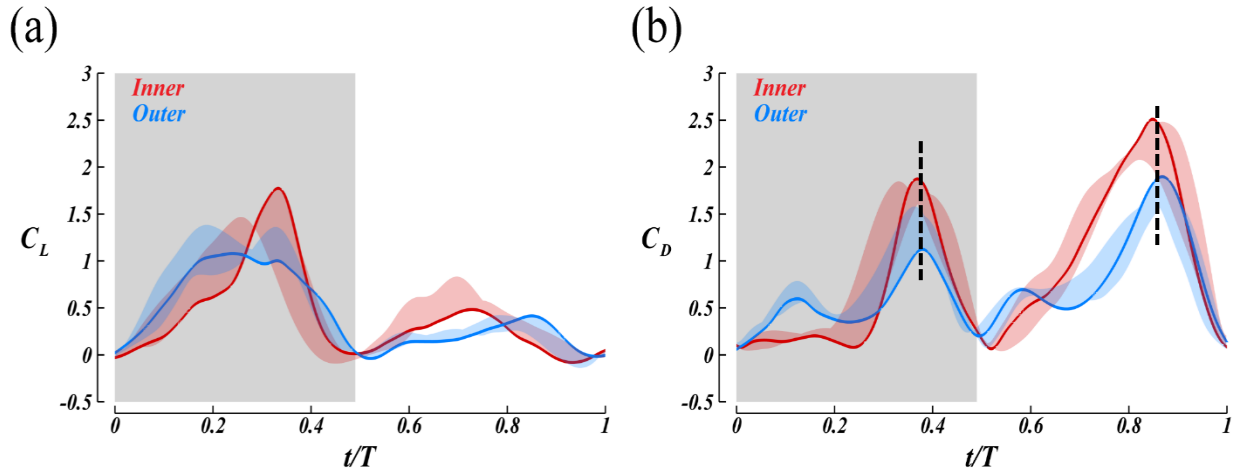


Figure 7. Time course of lift (a) and drag (b) coefficients during the turning phase of hummingbird pure yaw turn. The force coefficient histories over the 3rd stroke are shown in solid curves. Force coefficient differences for other strokes in the turning phase with respect to the 3rd stroke are shown as error bars. Red and blue correspond to the inner and outer wings, respectively. Shaded areas stand the downstrokes and unshaded areas stand the upstrokes.

Besides the lift force, horizontal force is also important in maneuvering flight since it can generate torque to drive the turn, especially for the pure yaw turn case. Figure 7(b) shows the drag coefficient history of this maneuvering flight. We can see from the plot that the horizontal force generated by the inner wing is always greater than that generated by the outer wing. Such force asymmetry in horizontal direction can accelerate the turn in downstroke and damps the turn in upstrokes. This half-cycle-based turning strategy is more flexible comparing to some other nature flyers, like the fruit flies, their wings always generate resultant torque towards the turning direction when they perform the maneuvering flight. It is much easier for the flyer to stop the turn and adopt an alternative flight motion based on what it needs, which is often the purpose of pure yaw turn.

The vortex formation over a stroke cycle (the 3rd stroke) is shown in Figure 8, in which the vortex structures are identified by the Isosurface of Q-criterion ($Q=10$). The vortex structures are colored by the non-dimensional pressure. The stroke cycle starts from the downstroke. Figure 8(a) shows the vortex structures at $t/T=0.24$, which corresponds to the peak of the vertical force during downstroke (Figure 8a). The most significant vortex structures at this moment is the formation of leading-edge-vortex (LEV). The LEV attaches well to the wing surface. More importantly, the LEV, the tip vortex (TV), the trailing-edge vortex (TEV), and the root vortex (RV) are connected end to end, forming a vortex loop, within which the air moves downward. A previously shed vortex loop (PVL) can also be observed. It was generated during the upstroke prior to this moment, and the PVL is connected to the newly formed vortex loop by the TEV. Similar vortex structures are found in hovering hummingbirds in previous studies [13-15].

As time advances to $t/T=0.33$, as shown in Figure 8(b), which corresponds to the peak of horizontal force in downstroke (Figure 8b), the wings are near the end of downstroke and rotate rapidly along their own axis. The outer wing LEV is divided into two branches, known as dual LEV [3], and two shed vortices, SLEV and STEV, can be identified. New vortex structures can be found at the outer side of the hummingbird for this time instance. The LEV, TV and STEV are connected with each other to form a vortex ring near the outer wing tip region. Also, the LEV, SLEV, TEV and RV are connected to form another vortex ring. It is worth noting that the directions of the vortex tube STEV and SLEV are opposite. Similarly, the PVL can be observed and it is connected to the later newly formed vortex ring. At the inner side of the hummingbird, the LEV develops and the newly formed vortex ring grow larger. However, the major vortex structures stay the same as we described at $t/T=0.24$.

At the end of the downstroke ($t/T=0.48$), as shown in Figure 8(c), the dual-ring vortex structure at the outer side of the hummingbird still can be observed. The vortices convect further downstream and the PVL starts to dissipate. The dual-ring vortex structure begins to merge to a single vortex ring.

During the upstroke ($t/T=0.73$), as shown in Figure 8(d), which corresponds to the peak of vertical force at upstroke (Figure 8a). The major vortex structures are similar to that at $t/T=0.24$, except for the more complex and stronger vortices due to larger angle of attack of the wings in upstroke (Figure 8c). At $t/T=0.88$, which corresponds to the peak of horizontal force at upstroke, the dual-ring vortex structure can be observed. Differently, it is the inner side of the hummingbird that presents the double loop vortex structure. At the end of upstroke, as shown in Figure 8(f), the dual-ring vortex structure still exists and the two vortex rings start to merge to a single vortex ring.

For all time instances discussed above, the inner side and outer side of the hummingbird show significant asymmetry in vortex wake structures. The unique dual-ring vortex structure exists in the outer side during downstroke and exists in the inner side during upstroke. Such dual-ring vortex structure is responsible for the wake asymmetry. The kinematic difference of the inner and outer wings may result in the unique dual-ring vortex structure, and further influence the wake structures of the inner and outer side of the hummingbird.

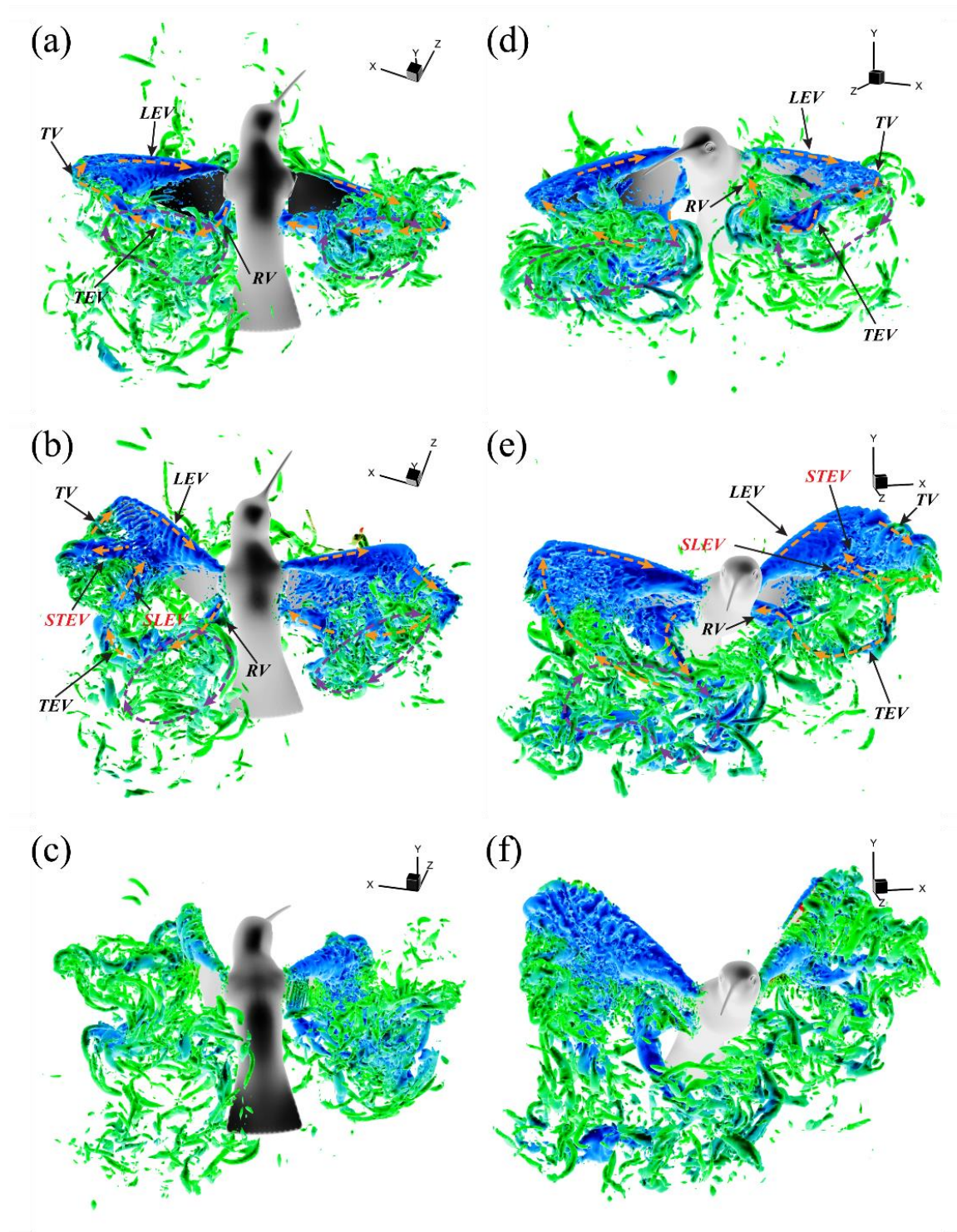


Figure 8. (a-f) Time course of vortex development of the 3rd stroke of the hummingbird pure yaw turn, visualized by the Q-criterion. The vortex structures are colored by non-dimensional pressure.

Concluding Remarks:

A three-dimensional direct numerical simulation was performed for a maneuvering hummingbird with a very accurate wing and body motion reconstructed from high-speed images. The simulation captures the aerodynamic force and power characteristics in the entire maneuvering process and also details of the flow field, including the unsteady wake structures in both near and far field. Our results on the maneuvering hummingbird kinematics suggest that hummingbird sustained yaw turns by tilting up the outer wing stroke plane and suppressing the outer wing figure eight motion; also by increase the wing pitching angle in downstroke and decrease the wing pitching angle in upstroke to create wing angle of attack asymmetry between inner and outer wings. For the wake structures, strong asymmetric wake topology is identified. More importantly, a unique dual-ring vortex structure, which is the source of the wake asymmetry, is found in the wake of one of the two wings of the hummingbird. The dual-ring vortex structure corresponds to larger wing twisting and lower drag production, which creates unbalanced aerodynamic forces to help with the maneuver.

(3) Computational investigation of cicada aerodynamics in forward flight

Many aerodynamic mechanisms of force generation by flapping wings have been proposed based upon studies on rigid mechanical models, including wing-wake interactions and rotational circulation[16], delayed stall during the translation portion of the stroke [17], axial flow stabilized leading edge vortex (LEV) [18], and rotational accelerations [19]. Although studies on wing models have substantially advanced the understanding of insect's flight, wing model has intrinsic restrictions such as wing rigidity and simplified kinematics. In this work, a realistic wing-body model a cicada (*Tibicen linnei*) is employed to investigate the aerodynamic performance and the wake patterns in insect forward flight.

The cicada flight is reconstructed using template-based hierarchical subdivision surface method. Marker points on the wings are digitized in each recorded image at each time step. As an example, Figure 9a shows a raw picture a cicada during downstroke. Figure 9b presents a comparison between a real cicada and the reconstructed result. Figure 10 shows the three Euler angle quantifying the flapping kinematics of the forewing and hindwing.

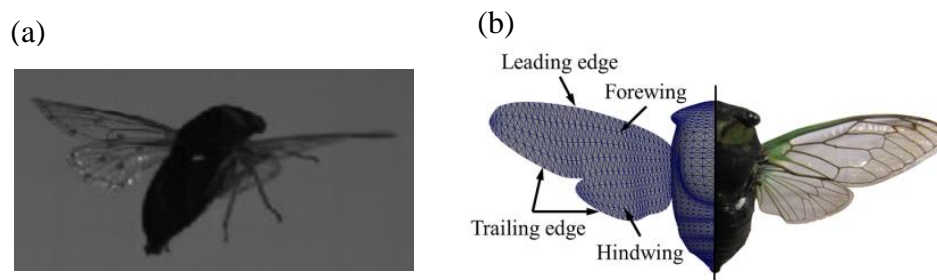


Figure 9. Real cicada and its reconstruction. (a) Raw picture; (b) Comparison of real and reconstructed cicada.

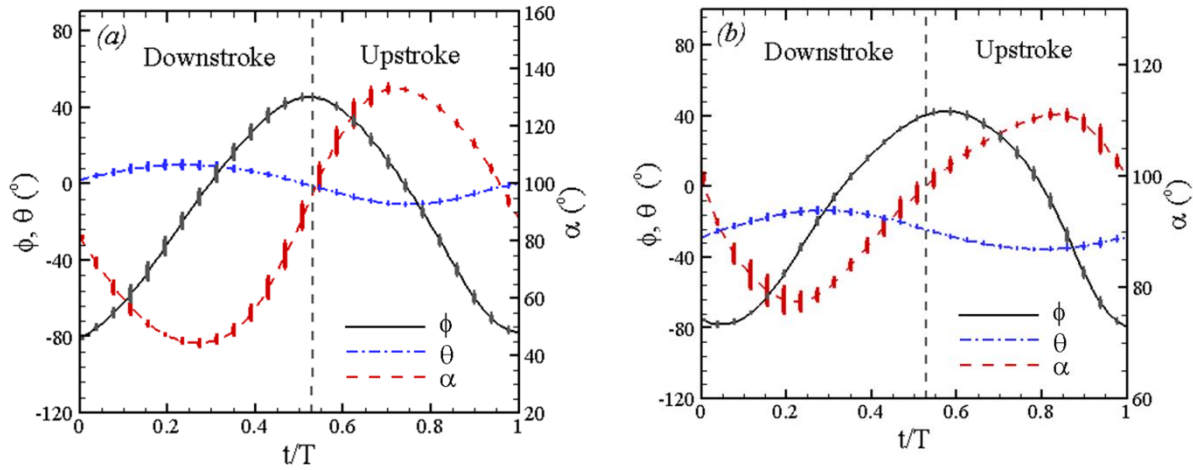


Figure 10. Stroke angle (0° lateral, downstroke positive), deviation angle (upward positive), and pitch angle (rotation around wing span, smaller than 90° when leading edge is forward) for the forewing (a) and the hindwing (b).

After the model is built, we carry out the high-fidelity simulation on the cicada forward flight. The vortex formation over a stroke cycle is shown in Figure 11, in which the vortex structures are identified by the iso-surface of Q -criterion ($Q=10$). At the onset of the downstroke (Figure 11a), an LEV is uniformly distributed along each leading edge. A forewing starting vortex (FSV) is formed along the extruded forewing trailing edge (partial of which is hooked with the leading edge of the hindwing). The LEV connects to the FSV through forewing tip vortex (FTV). On each hindwing, a trailing edge stopping vortex (TSV) is created and is about to be shed during the pronation. As wings further stroke down (Figure 11b), three-dimensional LEV develops due to the onset of wingtip vortices [20]. A hindwing starting vortex (HSV) forms at the hindwing trailing edge. Surrounding the cicada wing, the leading edge vortex, forewing tip vortex, and trailing edge vortices (FSV and HSV) all together form a horseshoe-like vortex structure. At the mid-downstroke (Figure 11c), the LEV is fully developed and a cone shape FTV is formed on the dorsal surface of the wing. The starting vortices (FSV and HSV) from the forewing and the hindwing are merged. Near the root of the hindwing, a wing root vortex (WRV) is generated on each side of the cicada. At the end of the downstroke (Figure 11d), the vortex rings are elongated. A strong tip vortex is developed from the hindwing (HTV), entangling with forewing tip vortices (FTV). At the mid-upstroke (Figure 11e), the vortices emanated from the posterior cicada body are elongated and intertwined with the wing root vortices. A stopping vortex (SV) shed forwardly during supination can also be seen. At the end of upstroke (Figure 11f), the vortex tube previously formed in the downstroke from the posterior cicada body has been detached, with each arm hooked to the vortex ring generated in the downstroke. Eventually, the vortex ring in each side of the body will merge with the PBV, and potentially form one big vortex ring after several stroke cycles.

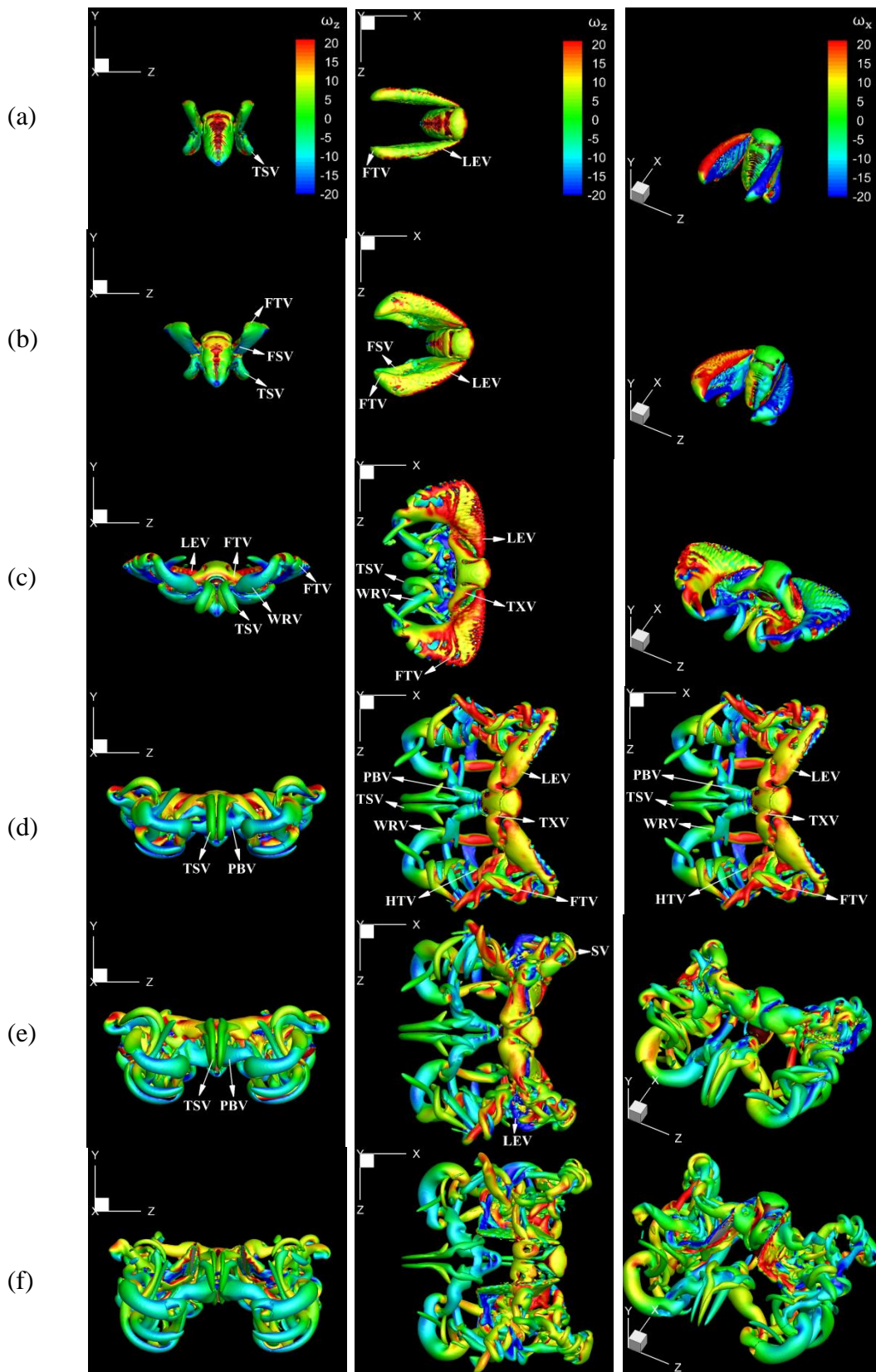


Figure 11. Time course of vortices development, visualized by Q-criterion. The left and middle columns are back view and top view respectively, and the vortex structures are colored by spanwise vorticity. The right column shows the structures in projection view, colored by streamwise vorticity. Color bars in the first row apply to figures in the same column.

Figure 12a shows the velocity vector and two-dimensional streamlines in a transverse plane cutting through the wing and part of the body. The LEV, TXV and WRV actually form a jet through which strong downwash flow is induced near the mid-wing region. Figure 12b is the velocity vector in a transverse plane half the body length behind the cicada, at which the trailing edge stopping vortices (TSV) are cut. The pair of TSV approaches to the center plane due to self-induction. The induced flow by TSVs can potentially enhance the formation and development of the wing root vortex, and therefore indirectly help the downwash. The wing root vortex induces upwash flow proximal to the hindwing and the body, but the affected region is far smaller than the estimated upwash region generated by bumblebees [21].

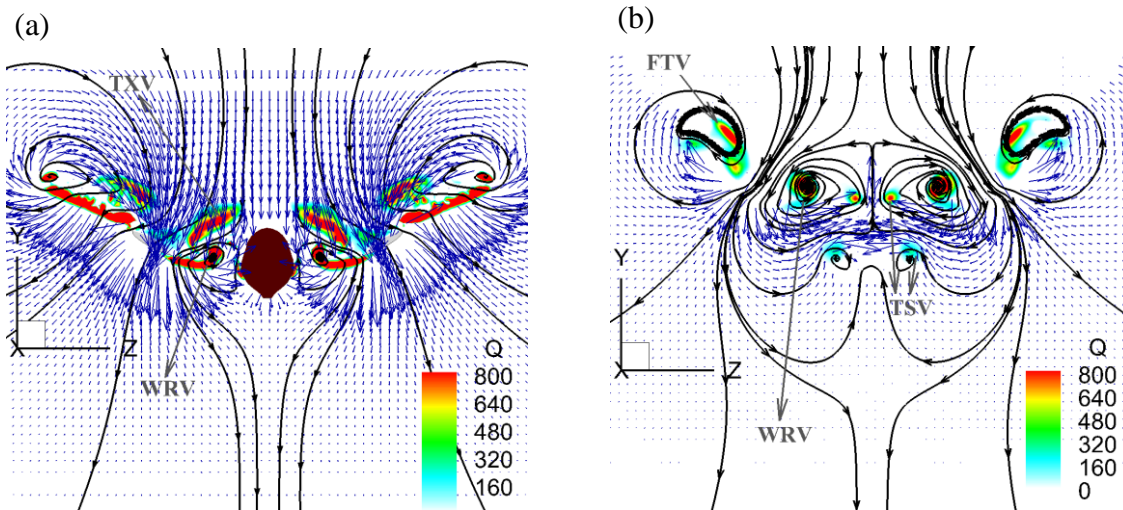


Figure 12. Transverse plane cut at mid-downstroke. (a) Cut through wing and body (b) Cut through the near wake (no wings or body being cut). Contour of Q-criterion, velocity vector, and two-dimensional streamline seen from the back view.

Concluding Remarks:

Free forward flight of cicadas is investigated through high speed photogrammetry, three-dimensional surface reconstruction and computational fluid dynamics simulations. We report two new vortices generated by the cicada body. One is the thorax generated vortex, which helps the downwash flow, indicating a new phenomenon of lift enhancement. Another is the cicada posterior body vortex, which entangles with the vortex ring composed of wing tip, trailing edge, and wing root vortices. Some other vortex features include: independently developed left and right hand side leading edge vortex, dual core leading edge vortex structure at the mid-wing region, and near wake two-vortex-ring structure. In the cicada forward flight, approximately 79% of the total lift is generated during the downstroke. Cicada wings experience drag in the downstroke, and generate thrust during the upstroke. Energetics study shows that the cicada in

free forward flight consumes much more power in the downstroke than in the upstroke, to provide enough lift to support the weight and to overcome drag to move forward.

(4) New lift enhancement mechanism of wing-body interaction in cicada forward flight

Following the above study, we further investigate the aerodynamic role of those body-generated vortices in cicada forward flight. A new lift enhancement mechanism, which is associated with wing-body interaction, is found. In this work, in order to examine the effects of WBI, two simplified models, WN (wings-only) and BD (body-only), are created based on the original reconstructed WB (wing-body) model. In the WN model, the same wing kinematics are kept as the WB model. For the BD model, only the body with the same inclination angle as that of the WB model is employed. By isolating the coupling of the body and wing models, we desire to investigate the inherent nature of body-involved unsteady force generation mechanism by comparing both aerodynamic performance and associated wake structures.

The comparisons of the instantaneous forces on the cicada body and the right wing are shown in Figure 13(a) and (b), respectively. In each plot, solid lines indicate simulation results from the WB case while dashed lines represent either the BD or WN model. The overall lift force produced by the wings and the body together is increased by about 18.7% according to Table 1, which suggests a significant aerodynamic benefit generated by WBI. This is mainly because of the lift increment on the cicada body, which contributes about 65% of the total lift enhancement. The body lift accounts for about 11.6% of the total lift generation in the WB model, whereas the body can only produce less than 2% of the total lift when separated from the wings and simulated under the same flow conditions. Therefore, the body plays a more important role in force generation when it interacts with the flapping wings.

Table 1. Cycle-averaged lift coefficient and its enhancement due to wing-body interaction.

\bar{C}_L	Single-wing	Body	Overall
WB	0.415	0.109	0.939
WN/BD	0.389	0.013	0.791
$\Delta\bar{C}_L$ (%)	6.7	738	18.7

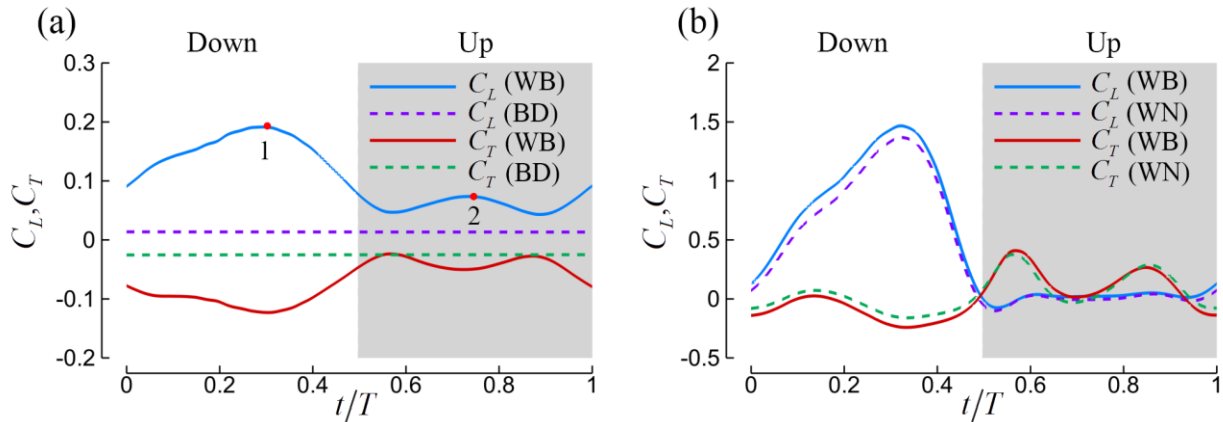


Figure 13. Time traces of lift and thrust coefficients of the body (a) and a single wing (b) during the fourth flapping cycle when both the aerodynamic forces and flow reach a periodic state. Peak 1 and 2 in figure (a) occur at $t/T=0.3$ and 0.74 , respectively.

Pressure distribution on the body and the wings are analysed. The pressure coefficient is defined as $C_p = (p - p_\infty) / 0.5 \rho U^2$, where p_∞ is the pressure in the freestream. The above force comparison indicates that the lift on the body increased a lot, so we plot the surface pressure on the body in Figure 14. Figure 14a is the pressure on the body in the WB model at $t/T=0.3$, at which the first peak of the body lift is observed. Two low-pressure regions on the thorax and posterior body can be clearly observed at this moment, which coincide with the locations of TXVs and PBVs, implying that they were generated by the two vortices. At the time instant $t/T=0.74$, at which the second lift peak occurs, the low-pressure regions generated by the PBVs disappears (Figure 14b), leaving only one low-pressure region on the body. This is because PBVs have already detached with the body. In addition, during upstroke, this low-pressure region moves to the top surface of the body and follows the movement of TXVs (Figure 14c). According to this analysis about the spacial and temporal change of the pressure on the body, the high body lift generated during downstroke is attributed to both TXVs and PBVs, while the lift peak which occurs at the mid-upstroke is mainly due to the TXVs.

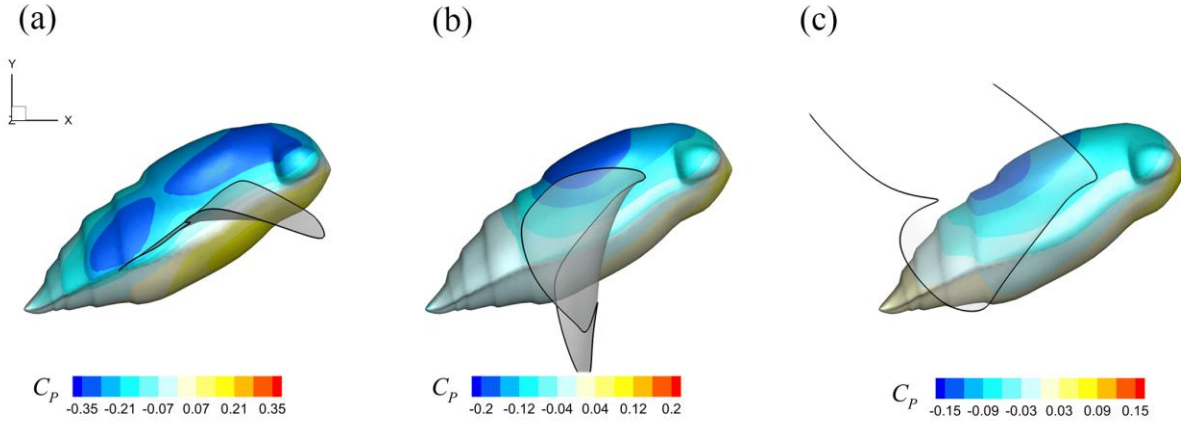


Figure 14. Surface pressure coefficient distribution on the body for the WB model at selected instants: (a) $t/T=0.3$; (b) $t/T=0.74$; (c) $t/T=0.9$.

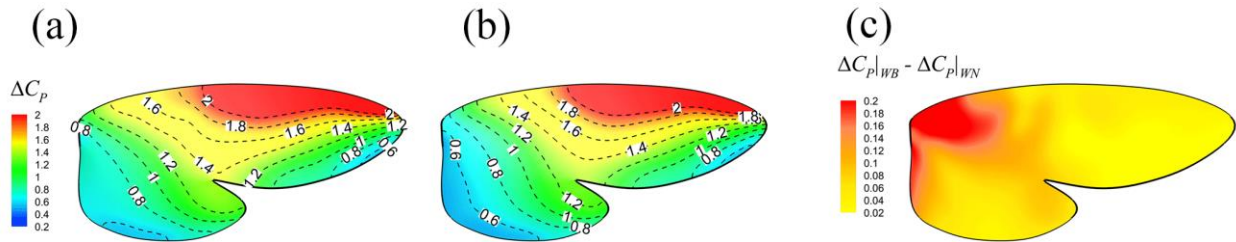


Figure 15. Pressure difference between the upper and lower wing surface (ΔC_p) of the right wing for the WB model (a) and WN model (b), respectively. (c) Shows the difference ΔC_p of between (a) and (b).

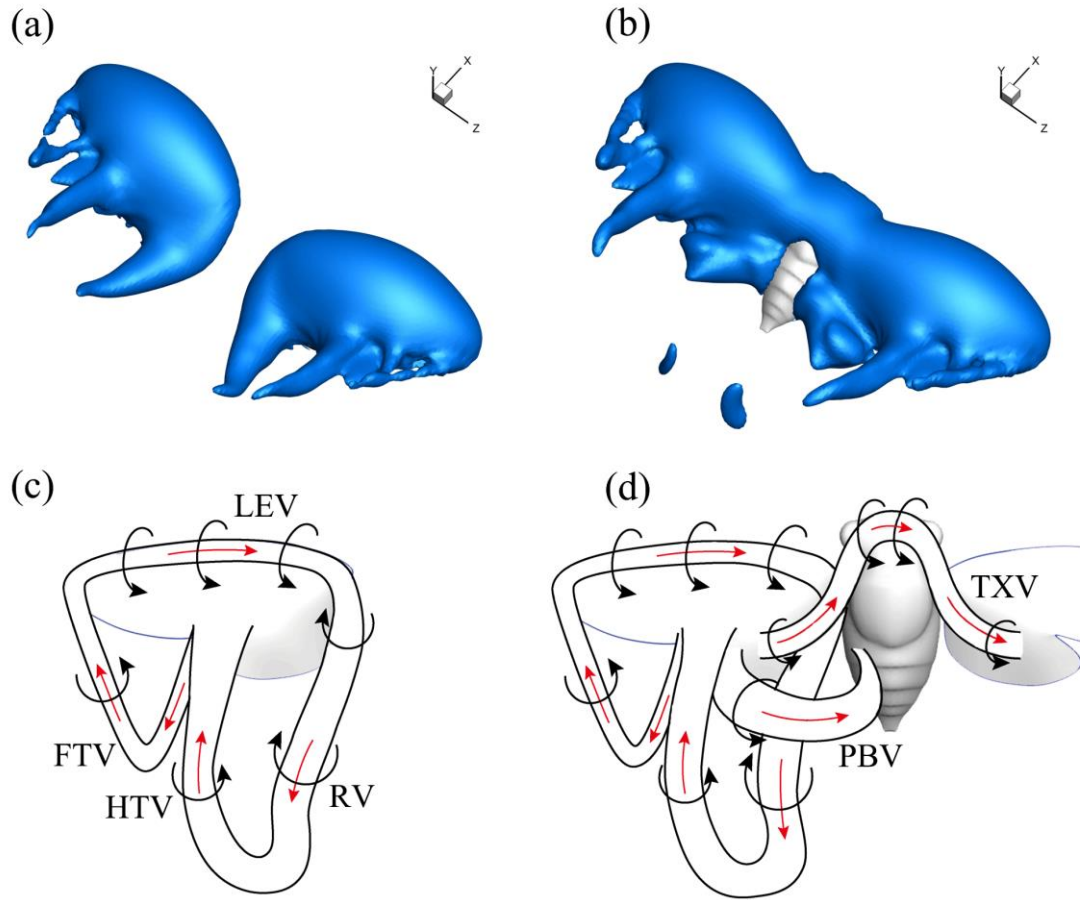


Figure 16. Isosurface of pressure coefficient ($C_p = -0.2$) at $t/T=0.3$ for (a) the WN model and (b) the WB model. Wake schematic for (c) the WN model and (d) the WB model at $t/T=0.3$.

To compare the surface pressure on the wing, we plot the difference of the pressure coefficient between the lower surface and the upper surface (ΔC_p) in Figure 15. Figure 15(a,b) indicate that the overall features of the pressure on the wing in WB and WN are similar. The outer half of the wing, especially on the leading-edge region, generates most of the lift force. The difference of ΔC_p between WB and WN is mainly located on the wing root region (see Figure 15c). An average 6.5% enhancement in wing lift production can be found in the WB model. This is attributed to the aforementioned enhancement of the strength of the LEVs near the wing root.

Isosurface contours of a low-pressure level have been plotted in Figure 16(a) and (b) for WN and WB, respectively, at $t/T=0.3$. Noticeable in both plots is a large region of low pressure right behind the wings which is due to the LEVs, RVs, forewing tip vortices (FTVs) and hindwing tip vortices (HTVs). However, for the WB model, an additional low-pressure region can be found behind the head and the thorax, which extends to the region between the sides of the abdomen and the hindwings. Figure 16(c) and (d) show the schematic of the correlation between vortex structures and regions of low pressure in Figure 16(a) and (b), respectively. The major vortical structures of the WN and WB models are identified. According to Figure 16, the extension of the

low-pressure region is due to the distinct and strong vortex structures, TXVs and PBVs, created by WBI. As a result, lift production on both the body and the wings were enhanced. More details about this work can be found in Ref. [22].

Concluding remarks

The effects of wing-body interaction (WBI) on aerodynamic performance and vortex dynamics have been numerically investigated in the forward flight of cicadas. Flapping wing kinematics was reconstructed based on the output of a high-speed camera system. Following the reconstruction of cicada flight, three models, wing-body (WB), body-only (BD) and wings-only (WN), were then developed and evaluated using an immersed-boundary-method-based incompressible Navier-Stokes equations solver. Results have shown that due to WBIs, the WB model had a 18.7% increase in total lift production compared with the lift generated in both the BD and WN models, and about 65% of this enhancement was attributed to the body. This resulted from a dramatic improvement of body lift production from 2% to 11.6% of the total lift produced by the wing-body system. Further analysis of the associated near-field and far-field vortex structures has shown that this lift enhancement was attributed to the formation of two distinct vortices shed from the thorax and the posterior of the insect, respectively, and their interactions with the flapping wings. Simulations are also used to examine the new lift enhancement mechanism over a range of minimum wing-body distances, reduced frequencies and body inclination angles. This work provides a new physical insight into the understanding of the body-involved lift-enhancement mechanism in insect forward flight.

(5) Aerodynamic effects of morphing wings in dragonfly forward flight

Although some encouraging progress have been made in advance our knowledge on flapping morphing wings [23-25], most of the previous studies are more focused on the aerodynamic performance rather than the vortical structures. So far, there is still a lack of qualitative and quantitative descriptions on the vortex formation of deformable wings, which can lead to improved models for the design of biomimetic propulsors, and also provide a better understand of vorticity transport mechanisms of morphing wings in nature. The present work is meant to fill some of the knowledge gaps in this regard. The high-speed photogrammetry system, 3-D surface reconstruction technology and numerical simulations are used to reveal the effects of morphing wings of a forward flight dragonfly. Specifically, the flapping morphing wing kinematics of a free-flight dragonfly are measured and quantified first (see Figure 17). We then use the reconstructed model (original case) to explore the effects of morphing wings, first by removing camber while keeping the same time-varying twist distribution (twist-only case), and second by removing both the camber and the spanwise twist (rigid case). Numerical simulations are carried out using an in-house immersed-boundary-method-based direct numerical simulation solver. To get a better understand of the aerodynamic roles of morphing wings, the leading-edge vortex, the wing surface pressure distribution, and wake structures were analyzed and compared in detail for the model wings.

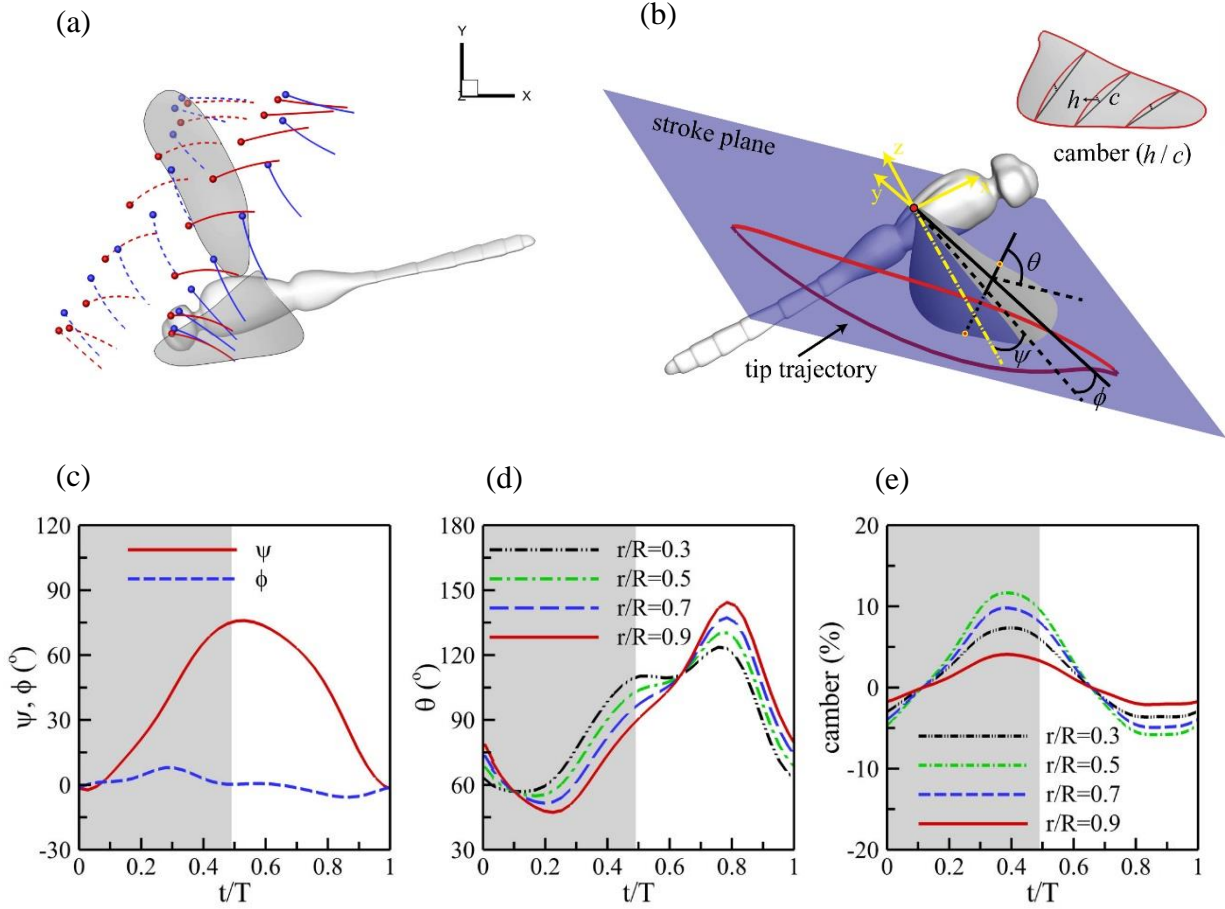


Figure 17. (a) Chord-lines of dragonfly forewing (dashed line) and hindwing (solid line) at a few instances. (b) Definition of wing orientation angles, wing stroke angle (ψ), wing deviation angle (ϕ), wing pitch angle (θ), and camber deformation (h/c). (c-e) Time course of wing kinematics of dragonfly hindwing. (c) Wing stroke angle (ψ) and wing deviation angle (ϕ). (d) and (e) are the wing pitch angles (θ) and camber deformation (h/c) of different sections along the wing span, respectively. The downstroke period is shaded as a gray color.

Using the above-reconstructed wing kinematics, the aerodynamic forces and power required for the flapping motion of three hindwing models were computed using the CFD solver, as shown in Figure 18. The stroke plane angle of hindwings were 77° with respect to the horizontal plane, which indicates that the hindwings flapped with nearly a vertical stroke. Therefore, the positive vertical force was typically created during the downstroke, and slight negative force was formed during the upstroke. The magnitude of the instantaneous vertical of the twist-only wing was smaller than that of the rigid wing, as clearly shown in the middle position of the stroke when the twist angle of the hindwing was largest. The instantaneous vertical force of the original wing with camber variation was similar to that of the twist-only wing during the downstroke. Due to the cruising motion, the force component in the horizontal direction is close to zero, and only slight thrust was produced for compensating the body friction drag during the upstroke. The aerodynamic power consumption in the plot shows that the rigid wing requires more energy for flapping in comparison with the other models.

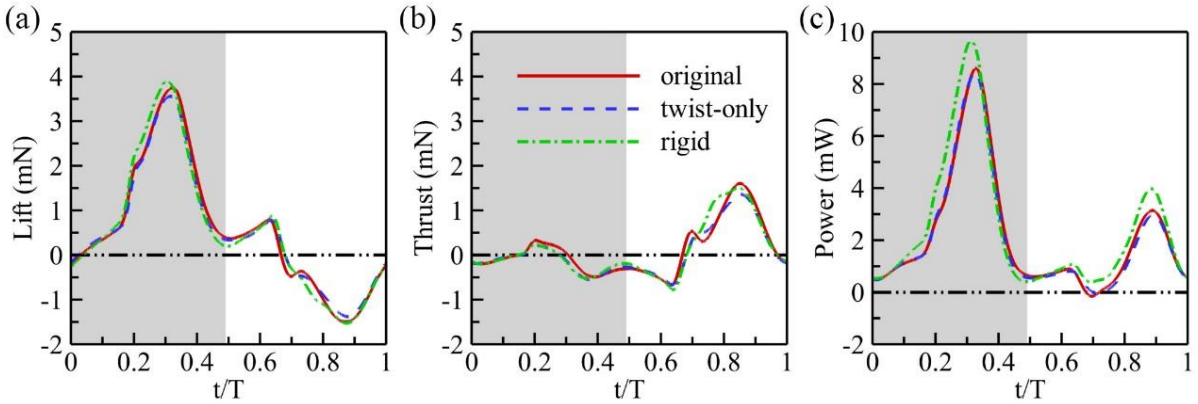


Figure 18. Time course of lift (a), thrust (b) and power (c) of the hindwing.

Concluding remark

More details about this work can be found in Ref. [26]. Major contributions are summarized as follows. In this study, a high-speed photogrammetry system, 3-D surface reconstruction technology and numerical simulations are used to reveal the effects of morphing wings of a cruising dragonfly. Specifically, the flapping morphing wing kinematics of a free-flight dragonfly are measured and quantified first. We then used the reconstructed model to explore the effects of morphing wings, first by removing camber while keeping the same time-varying twist distribution, and second by removing both the camber and the spanwise twist. Our simulation results revealed that the surface deformation can improve the aerodynamic functions in two ways: 1) improving the power economy by preventing the tip vortex bursting; and 2) improving the leading-edge vortex attachment by suppressing the generation of the secondary vortex. As a result, the spanwise twist can boost the aerodynamic efficiency up to 20%, especially during the wing translational phase.

(6) Aerodynamics of a dragonfly turning maneuver

Clever maneuvers can be commonly observed in insect flight for capturing food and/or avoiding predators. Unlike most other insects such as flies, wasps and cicadas either reduced their hind-wings or mechanically coupled fore and hind wings, dragonflies have maintained two independent-controlled pairs of wings throughout their evolution [27]. Their neuromuscular system allows them to actively change many aspects of wing motion in a single wing, such as the angle of attack, stroke amplitude, and stroke plane. Most previous studies of are focused on the aerodynamics of dragonfly-like tandem wings in steady flight motion. Although the unsteady free flights of dragonflies have also been studies [28-30], their works were limited on reporting the wing kinematics and associated flight dynamics. The present effort is meant to fill some of the knowledge gaps in this regard. Specially, a high-speed photogrammetry system and 3-D surface reconstruction technology [1] are used to reveal dragonfly wing kinematics during a

turning maneuver flight (see Figure 19). The aerodynamic performance and the flow structures (see Figure 20) is then studied using an in-house immersed-boundary-method-based computational fluid dynamics (CFD) solver. This work aims to investigate the aerodynamic characteristics of forewings and hindwings and its associated forewing-hindwing interaction effects in a turning maneuvering motion.

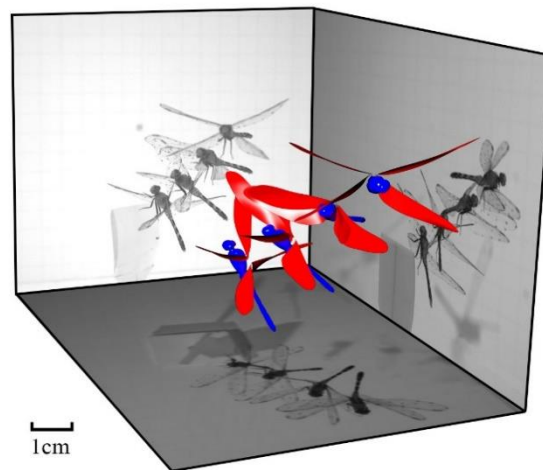


Figure 19. Motion reconstruction of dragonfly taking-off maneuver. The side panels show 4 of 110 frames recorded by high-speed videography.

More details about this work can be found in Ref. [26]. Major contributions are summarized as follows. The asymmetrical wing kinematics generate unbalanced forces in both vertical and horizontal directions. During the downstroke, the force generated by the outer wings are higher than inner wings. By contrast, the inner wings generate higher forces during the upstroke. The surface pressure distribution shows that the majority of the force is generated around the leading-edge. The unbalanced forces lead to the torques along its body axis in three directions. Specifically, both forewings and hindwing contribute to the roll torque generation, whereas forewings are dominant in generating pitch and yaw torques. To examine the effect of forewing-hindwing interaction on the aerodynamic performance, two additional cases, one with forewings only and the other with hindwings only, are carried out. Our results indicate that the interaction can lead to a slight forces reduction, but can save the aerodynamic power up to 11%.

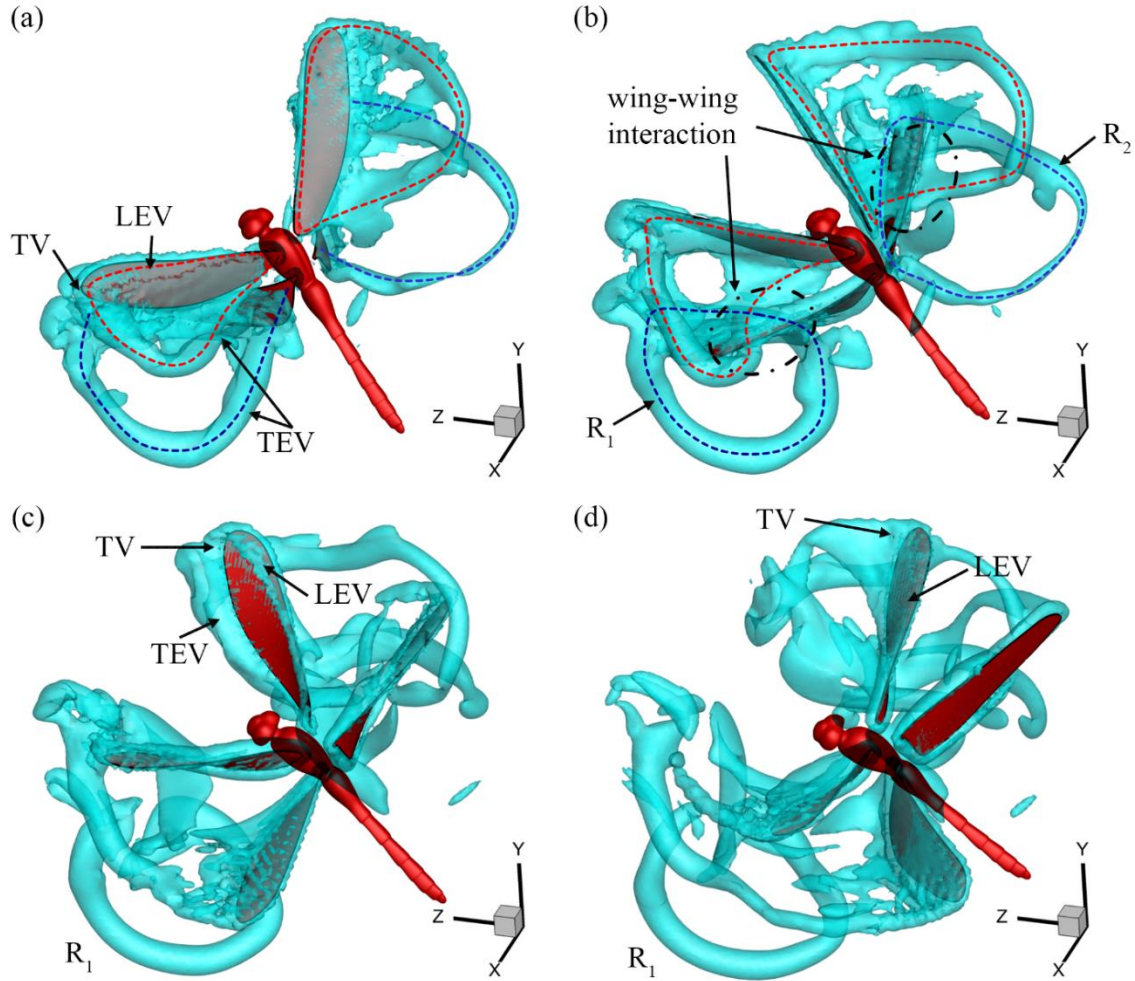


Figure 20. 3-D vortex structures in the flow during the early turning motion, where the time stamp from (a) to (d) is 23, 29, 35 and 40 ms. The vortex loop from the downstroke is marked by dashed.

2.3 Low-dimensional Modeling and Analysis of the Morphing Wing Kinematics

1) Spherical-coordinates-based Singular Value Decomposition (SSVD)

Singular value decomposition (SVD, also known as POD or PCA in some fields of application) is a powerful method for data analysis aimed at obtaining low-dimensional approximate descriptions of a high-dimensional process or dataset [31]. The most remarkable feature of the SVD is its optimality: it provides the most efficient way of capturing the dominant components of any dataset with only a finite and often surprisingly few numbers of modes. In gait analysis, PCA has yielded insights into human walking strategies and the interrelationships in terms of temporal, kinematic and kinetic variables. Urtasun and colleagues [32] have used

PCA to identify invariant or common features within the whole body kinematics of a contemporary dance movement pattern. For animals in nature, Bozkurtas and colleagues [33] have used SVD to study the pectoral fin kinematics and its associated aerodynamics of bluegill sunfish. Representing the motions as a linear sum of principal components has become a widely accepted animation technique [34, 35]. SVD and other similar methods are closely related, and the close connections and equivalence of these various methods can be found elsewhere [31].

SVD can be considered as an extension of the traditional eigenvalue decomposition for the non-square matrix, which contains dataset that represent the wing motion in both time and space. Displacements of all m nodes on the wing surface at n distinct instants in time are stored in this matrix, named displacement matrix. The displacement matrix (denoted by \mathbf{A}) is as follows:

$$\mathbf{A} = \begin{bmatrix} \Delta r_1^1 & \Delta r_1^2 & \cdots & \Delta r_1^n \\ \Delta \theta_1^1 & \Delta \theta_1^2 & \cdots & \Delta \theta_1^n \\ \Delta \phi_1^1 & \Delta \phi_1^2 & \cdots & \Delta \phi_1^n \\ \vdots & \vdots & \vdots & \vdots \\ \Delta r_m^1 & \Delta r_m^2 & \cdots & \Delta r_m^n \\ \Delta \theta_m^1 & \Delta \theta_m^2 & \cdots & \Delta \theta_m^n \\ \Delta \phi_m^1 & \Delta \phi_m^2 & \cdots & \Delta \phi_m^n \end{bmatrix}_{3m \times n} \quad (8)$$

The displacements stored in above matrix are calculated as follows:

$$\begin{cases} \Delta r_i^t = r_i^t - r_i^{ref} \\ \Delta \theta_i^t = \theta_i^t - \theta_i^{ref} \\ \Delta \phi_i^t = \phi_i^t - \phi_i^{ref} \end{cases} \quad (9)$$

where $(r_s^t, \theta_s^t, \phi_s^t)$ denote the coordinates of the node s at time instant t . Note that the spherical coordinate system is used here. $(r_i^{ref}, \theta_i^{ref}, \phi_i^{ref})$ denote the coordinates of the node i at a specific reference time instant. An SVD of the displacement matrix \mathbf{A} can then be factorized as

$$\mathbf{A}_{3m \times n} = \mathbf{U}_{3m \times 3m} \mathbf{S}_{3m \times n} \mathbf{V}_{n \times n}^T \quad (10)$$

where $\mathbf{U}_{3m \times 3m}$ and $\mathbf{V}_{n \times n}^T$ are two orthogonal unitary matrices; $\mathbf{S}_{3m \times n}$ is a diagonal matrix in which the diagonal values are called the singular values of \mathbf{A} , which are unique. The diagonal elements \mathbf{S}_{ii} consist of $r = \min(m, n)$ non-negative numbers λ_i , which are arranged in descending order, i.e. $\lambda_1 \geq \lambda_2 \geq \cdots \geq \lambda_n \geq 0$. Within the SSVD procedure, the λ_i values are the square roots of the eigenvalues of $\mathbf{A}\mathbf{A}^T$, whereas the eigenvectors of $\mathbf{A}\mathbf{A}^T$ make up the columns of \mathbf{U} and \mathbf{V}^T respectively. In the above expression, \mathbf{V} represents the change in each mode with time, and \mathbf{U} contains the eigenvectors corresponding to the spatial distribution of the modes. The singular values λ_i can be interpreted as the weight contributions of each mode in the SSVD. Thus, the ‘shape’ of any particular mode (say the k^{th} mode) can be extracted by zeroing out all the singular values except for the k^{th} value, and reconstructing from the SVD as in Eqn(10). Similarly, lower dimensional (say rank $K < n$) approximations to the dataset can be obtained by using an approximation to \mathbf{S} denoted by \mathbf{S}_K wherein $\lambda_{K+1} = \lambda_{K+2} = \cdots = \lambda_n = 0$ and reconstructing from the SSVD as follows:

$$\mathbf{A}_K = \mathbf{U} \mathbf{S}_K \mathbf{V}^T \quad (11)$$

2) Low-dimensional Morphology Analysis of Flapping Wing Flight in Nature

In this section, we will first show details of the SSVD for the forewing motion of a hovering dragonfly. The displacement matrix \mathbf{A} is now subjected to SSVD. In the following part, the forewing motion of a hovering dragonfly will be used to demonstrate the decomposition results. 30 snapshots of the wing motion for one complete flapping cycle are used in the decomposition. As expected, the SSVD leads to 30 distinct singular values, and the spectrum for the first ten singular values of the wing motion is shown in Figure 21 along with a cumulative plot for the same data. The normalized singular value for k^{th} mode λ_k^* is defined as:

$$\lambda_k^* = \lambda_k / \sum_{i=1}^n \lambda_i \quad (12)$$

The singular values are normalized by the sum of all singular values. Therefore, the cumulative values sum to unity. A number of interesting observations can be made from this plot. First, the singular value spectrum shows three distinct ranges: the first between mode 1 - 2, in which we see a rapid decrease in the amplitude, the second from mode 2 - 4 in which there is a much slower reduction in amplitude and, finally, the range from mode 4 - 30 that has negligible (less than 2%) total contribution. The rapid initial decrease in the spectrum is significant which suggests that a small number of modes contain most of the essential features of the wing gait. In fact, the cumulative values show that the first two and three modes capture about 93.1% and 96.0% respectively of the total motion. In fact, only the first mode captures close to 84.7% of the motion of the wing, which is a clear demonstration of the ability of SSVD to represent the dataset with the least possible number of modes.

The gait corresponding to individual modes can be extracted as described above, and the surface conformations for each of these extracted modes are then constructed using the original wing mesh with triangular elements. The first two modes are highly distinct and relatively easy to interpret, and we briefly describe the key qualitative features of these modes. Figure 22(b, c) shows mode 1 and mode 2 at five different times during one flapping cycle. Also shown on the left for direct comparison are the wing motion from the experiment (also called the ‘mode-all’ case, since it contains all the SSVD modes). In these figures, the colors reflect wing deformation by plotting contours of distances between vertices on the wing surface to the corresponding least square plane of the wing. Mode 1 involves very large rotating motion about the wing root, which is called the ‘flapping’ motion. The wing flaps back and forth with certain offset angle. And also, the mode one shows minimum deformation during the stroke. This mode is actively produced by the dragonfly through flight muscles at the wing root.

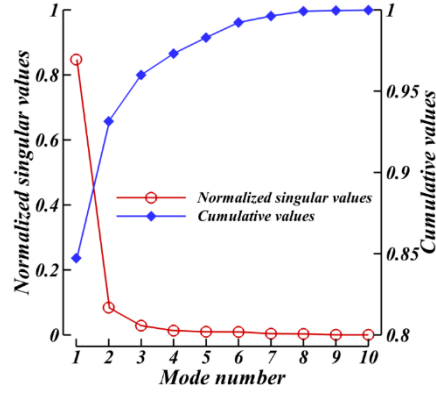


Figure 21. The SSVD spectrum of the first ten modes for the dragonfly right forewing kinematics. The left ordinate shows $|\lambda_i| / \sum |\lambda_i|$, and the right ordinate shows the cumulative value of the left ordinate.

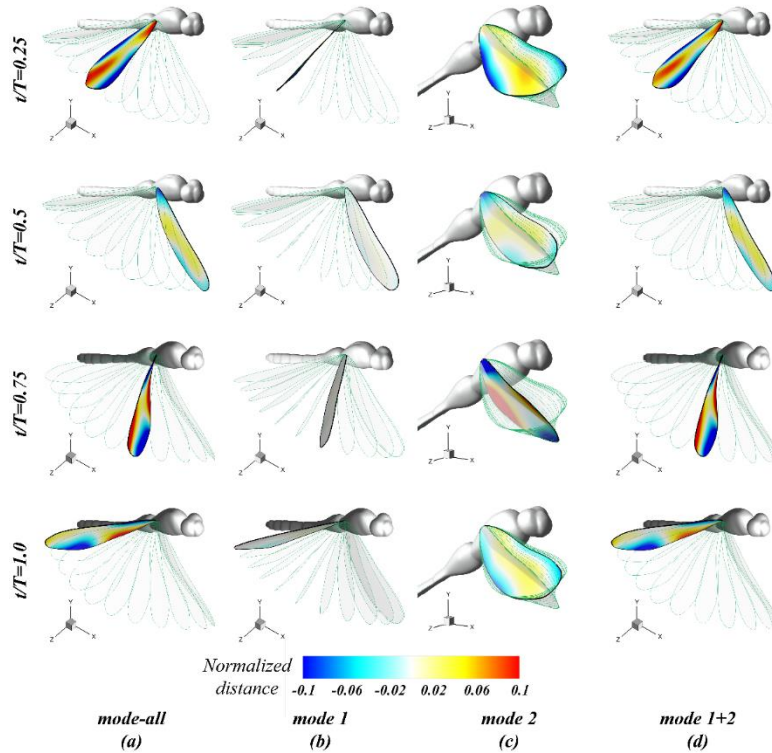


Figure 22. Wing motions of (a) experimental kinematics (also called the mode-all case), (b) SSVD mode 1, (c) mode 2 and (d) low-dimensional model mode 1+2. The wings are colored with distances between wing surfaces and corresponding least square planes. The distances are normalized by wing mid chord length.

Mode 2 is a twisted motion primarily in the span-wise direction, which occurs along the span axis of the wing. It presents as chord-wise rotations of the wing during the reversal phase. In contrast to mode 1, this mode is primarily a result of flow-induced deformation. It can be deduced from the fact that there are no muscles in the wing surface that could produce

deformation in the wing. Furthermore, the deformation is primarily in the direction of the flow relative to the wing motion, which supports the assertion that this mode is flow-induced. The rest of the modes in the spectrum are associated with relatively small motions that are not very distinct. We, therefore, do not describe these individually, although we will consider the effect of mode 3 on the aerodynamics in the following sections.

SSVD has decomposed the wing motion into its orthogonal components and helped us understand the key features of the nature flyers wing motion. The SSVD results can also be used to reconstruct low-dimensional approximations of the mode-all case using a subset of the orthogonal modes. Lower dimensional models of the wing gait are synthesized by successively adding modes to Mode 1. The forewing motion of a hovering dragonfly is used to demonstrate the method. Figure 22(a, b, d) shows the surface snapshots at four different time instances during one flapping cycle for mode 1 and mode 1+2 in comparison to the complete (mode-all) motion. The similarity between the wing shapes for Mode 1+2 and the Mode-All/experiment cases is evident in this figure. Removal of higher SSVD modes from the motion is analogous to filtering the experimental data in space and time.

The SSVD analysis suggests one natural approach to the development of the robotic wing. Since a small number of modes capture a significant portion of the motion, it stands to reason that a systematic procedure for developing a robotic wing would involve designing actuation mechanisms that reproduce a small number of these modes. The question that remains to be answered is what kind of performance can we expect from these lower dimensional wing models, and how does the performance scale as we include additional modes? This will allow us to make a rational compromise between the complexity of wing design and wing performance. It should be noted here that the performance is a consequence of the flow associated with these low-dimensional wing models. Thus, even though the modes are kinematically linear (and therefore additive), the performances are not expected to scale linearly with the modes since the flow is governed by the Navier-Stokes equations that are nonlinear. Thus, the answer to the above question requires that we explicitly determine the performances for these low-dimensional wing models. The following sections describes our approach to answering this question.

We further study the effects of increasing the dimensionality of the forewing motion of the hovering dragonfly on the aerodynamic performances. The effects of model dimensionality on the quantitative characteristics of the wing are investigated, including force production and lift economy.

The time variations of lift, drag and power coefficients are presented for all the low-dimensional gaits and compared to the mode-all case in Figure 23(a - c), respectively. Several observations on how each SSVD mode contributes to the performances of the wing can be made from these results. It should be noted that only mode 1 can be simulated by itself. However, given the underlying nonlinearity of the flow, the contribution of mode 2 and mode 3 are investigated by considering the differences in the performances from the lower-level gait. Thus, the effect of mode 2 on performance is obtained by analyzing the differences between the performances of the mode 1 and mode 1+2 cases. Similarly, the effect of mode 3 on wing performances can be assessed by comparing the performances of the mode 1+2+3 case with that of the mode 1+2 case.

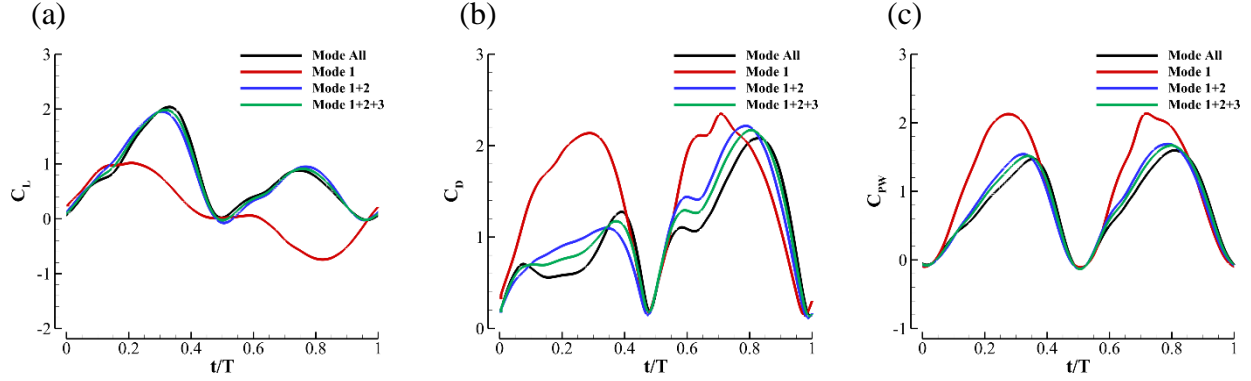


Figure 23. Comparison of the time variation of aerodynamic performances between the mode-all and low-dimensional gaits. (a) lift; (b) drag; (c) power.

Table 2. Cycle averaged aerodynamic performance of the mode-all and low-dimensional gaits.

	λ^* (%)	$\overline{C_L}$	$\overline{C_D}$	$\overline{C_{PW}}$	η	Lift production (%)
Mode-all	100	0.752	1.021	0.776	0.969	100
Mode 1	84.7	0.149	1.464	1.087	0.137	19.8
Mode 1+2	93.1	0.749	1.100	0.818	0.916	99.6
Mode 1+2+3	96.0	0.750	1.082	0.813	0.923	99.7

As we can see in Figure 23 that the aerodynamic performances are very similar for all cases except for the mode 1 only case. For the lift production, Figure 23(a) shows that all cases produce positive lift except for mode 1 case, which negative lift can be observed during the upstroke. Also, the lift production for mode 1 case during downstroke is much smaller (about 2.5 times smaller) than other cases. For the drag production, Figure 23(b) shows that the drag is much higher for mode 1 only case during the downstroke. For upstroke, the drag productions are very similar for all cases. These are because the lack of wing rotation about the span axis, which is included in the deformation mode (mode 2). During the downstroke, the wing angle of attack for mode 1 case is much greater than other cases, and it leads to less lift and more drag production (Figure 23b). During the upstroke, the wing angle of attack for mode 1 case is greater than 90 degrees due to lack of wing rotation about the span axis, and negative lift produces at this phase. The involvement of the deformation mode (mode 2) can greatly improve the lift production and reduce the drag produced by the wing.

For the aerodynamic power histories (Figure 23c), we can see that all cases present two peaks during the cycle, and the amplitude of power consumption for mode 1 case is much greater than other cases at both down and upstrokes. This suggests that involving the deformation mode (mode 2) can also reduce the power consumption of the dragonfly.

Cycle averaged aerodynamic performances are listed in Table 2. We can see from the table that mode 1+2 is a good approximation of the original wing motions mode-all. It contains only two dominant SSVD modes, and the motion is recovered over 90%. The associate aerodynamic

performances of mode 1+2 case are very similar to the mode-all case as. The lift production is recovered 93% of the original motion.

For the wake structures, we cut slices along the wingspan to see the leading edge vortex structures and measure the associated circulations evaluated at each slice. Figure 24 shows the corresponding results. We can see from the figure that for all cases, the LEV shapes gradually grow bigger from the wing root to wing tip. More importantly, the corresponding vortex structures are very different in mode 1 only case comparing to other cases. The LEV shapes are much bigger, and the associated attachment is bad in mode 1 case. For other cases, the LEV shapes are similar. Small differences can be observed near the wing tip region. At mid downstroke ($t/T=0.25$), the LEV attachment is pretty good for all cases except for the mode 1 only case. However, at mid upstroke ($t/T=0.75$), the LEV attachment is not as good as that at mid downstroke.

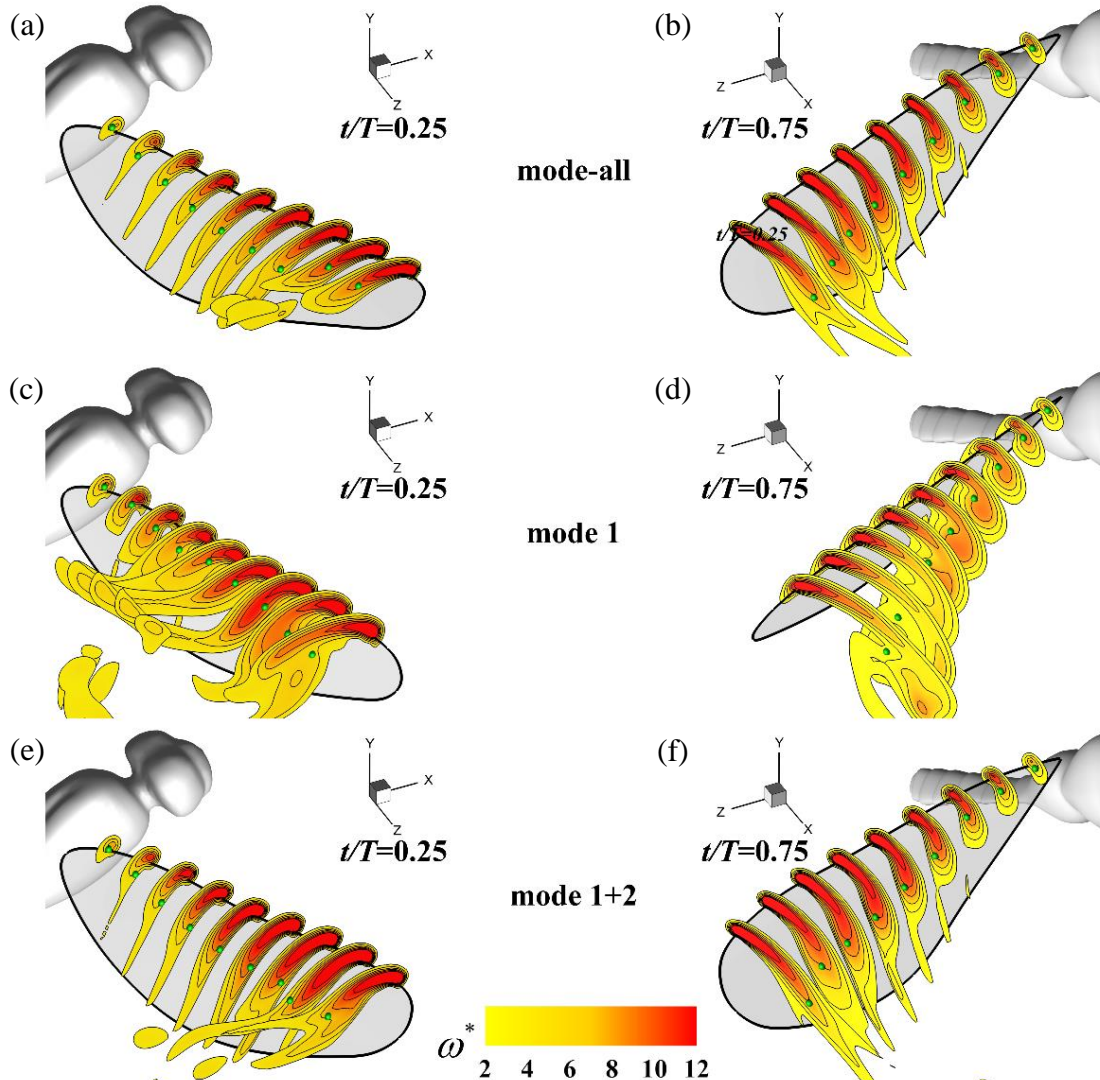


Figure 24. 2D slices of the leading edge vortex along the wingspan (10%~90%) at two time instances for (a, b) mode-all, (c, d) mode 1, and (e, f) mode 1+2 cases. The corresponding vortex center are marked with green dots at each slice. The contours represent normalized span-wise vorticity.

Quantitative measurements related to the LEV attachments of all cases discussed above are conducted. We first determine the LEV centers based on vortex shapes shown in Figure 24. After that, we measure the distances, which are named as lift-off distances, between LEV centers (green dots) and the wing surface to evaluate the LEV attachments. Figure 25 shows the results at mid downstroke ($t/T=0.25$) and mid upstroke ($t/T=0.75$). For the mode 1 only case, the lift-off distances are much higher than other cases in both time instances, which indicates bad LEV attachment. In addition, the ranges of the lift-off distance are much wider in mode 1 only case for both time instances. It ranges from 0.15 chords to 0.55 chords at mid downstroke, and from 0.20 chords to 1.09 chords at mid upstroke. Moreover, at mid downstroke, a small peak of lift-off distance shows up at 60% span and then drops at 70% span, which corresponds to the shed of LEV at 70% span in Figure 24(c).

For the mode-all and mode 1+2 cases, the lift-off distances are quite similar. The differences are less than 8% and 10% for each span location at mid downstroke and mid upstroke, respectively. More importantly, at both time instances, two distinct ranges of the lift-off distances can be observed. The first range is from 10% to 60% span, where the lift-off distance increases slowly. It suggests that the LEV attached pretty well with this range. The second range is from 60% to 90% span, where a rapid increase in lift-off distance can be observed. The LEV is lifted by the tip vortex and starts to merges with the tip vortex at this point.

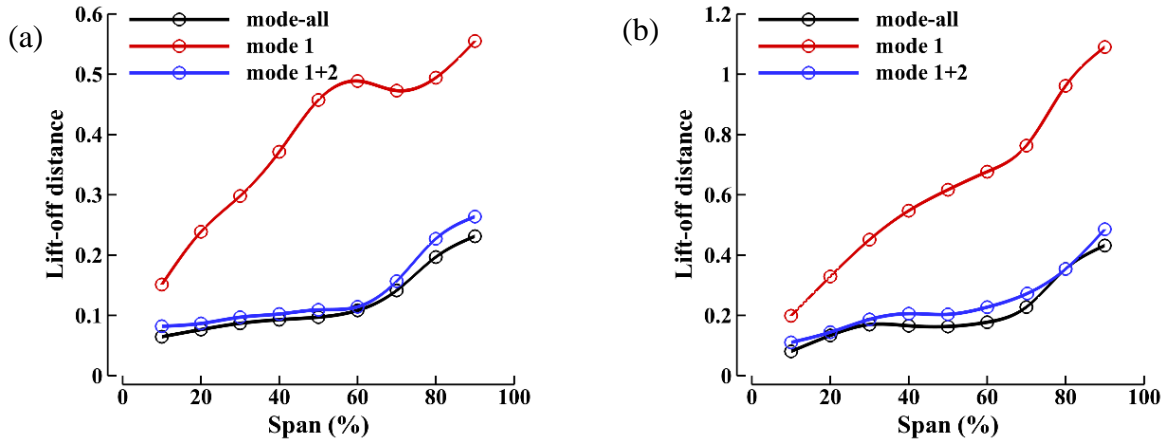


Figure 25. Distances of LEV center to the wing surface (lift-off distances) at (a) $t/T=0.25$ and (b) $t/T=0.75$ for mode-all, mode 1, and mode 1+2 cases.

The lift-off distances at mid downstroke are almost twice as much as that at mid upstroke for all cases and span locations, which indicates that the LEV attachment at downstroke is much better than upstroke.

Quantitative measurements of LEV circulation distributions along the wingspan are also performed for all cases discussed above based on the 2D flow slices shown in Figure 24. Figure 26 shows the corresponding results at mid downstroke ($t/T=0.25$) and mid upstroke ($t/T=0.75$). The circulation is calculated and normalized as follows:

$$\Gamma^* = \frac{c}{U_{ref}} \iint_S \omega \cdot d\mathbf{S} \quad (13)$$

Where S stands the surface of LEV shapes shown in Figure 24; ω is vorticity on S ; U_{ref} is reference velocity, which is chosen as the average velocity of wing mid chord; c denotes the mid

chord length. We can see from Figure 26 that the LEV circulations of mode-all, mode 1+2 and mode 1+2+3 cases are very close. The difference is less than 7% at mid downstroke and 3% at mid upstroke. For all cases, the LEV circulations gradually increase from the wing root to wing tip and drops a little bit near the wing tip region. Maximum circulation can be observed at around 80% span, and the corresponding value for mode 1 only case is about 1.5 and 1.3 times larger than that of other three cases at mid downstroke and mid upstroke, respectively.

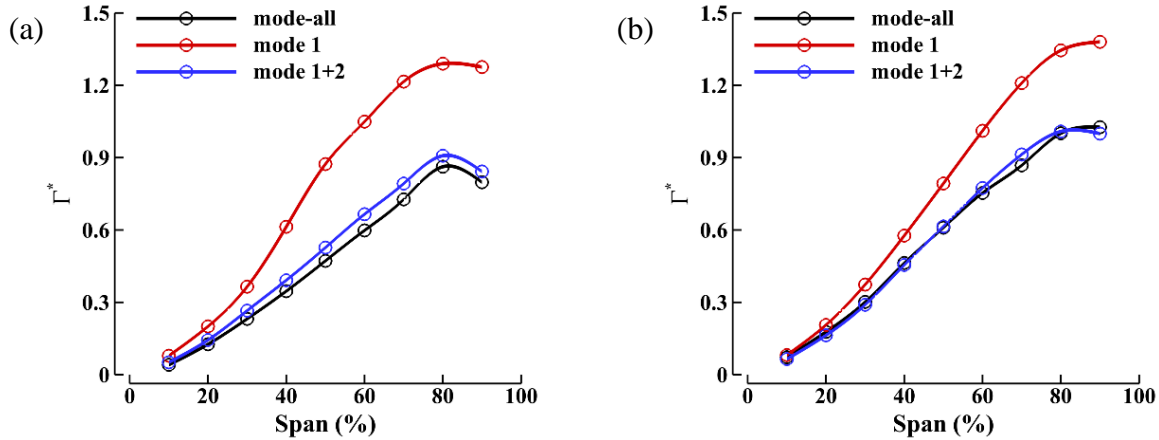


Figure 26. LEV circulations at (a) $t/T=0.25$ and (b) $t/T=0.75$ for mode-all, mode 1, and mode 1+2 cases.

In summary, we have studied three-dimensional flows around the forewing of a hovering dragonfly in this section, focusing on the effects of model dimensionality. Both qualitative observations and quantitative measurements are performed. The results show that for cases of mode-all, mode 1+2 and mode 1+2+3, the wake structures in both far and near field are similar, while significant differences can be found in mode 1 only case. Quantitative measurements of the flow field at two time instances ($t/T=0.25$ and 0.75) are performed in all cases, including the LEV lift-off distances and circulations. The results show the similarity in all cases except for the mode 1 only case, which has much greater LEV lift-off distances and circulations.

Concluding Remarks:

In this work, a combined experimental and computational method is developed to study the complex morphing wing kinematics and its associated aerodynamics of a hovering dragonfly. SSVD analysis shows that the wing motion can be described by only three dominant modes. The first two dominant modes, which contain 93.1% of the total motion, are highly distinguishable. The mode 1 (flapping mode) consists of a simple flapping motion, and the mode 2 (morphing mode) contains morphing in span-wise and chord-wise directions. The simulation results show that with the help of the mode 2, the lift production and lift economy are greatly improved comparing to the mode 1 only case. Also, the mode 1+2 case can recover 96% of the lift production and 91% of the lift economy of the original case. By studying the unsteady flow field of all cases, we conclude that the SSVD mode 2 can greatly reduce the large tip vortex found in the mode 1 only case. In addition, the leading edge vortex attachment is greatly improved for the cases with the mode 2.

2.4 Optimization of Low-dimensional Morphing Wing Models

In this section, we investigate the optimal configurations of dominant modes on aerodynamic performance for the dragonfly wing. Figure 27 shows the convergence histories of the three design variables, W_1 , W_2 , and φ . The objective functions are chosen as the cycle averaged lift coefficient and the lift efficiency. The initial guesses of the design variables correspond to the low dimensional model Mode 1+2 ($W_1=1$, $W_2=1$, and $\varphi=0^\circ$). We can see from the figure that the two optimization case converge within 6 iterations.

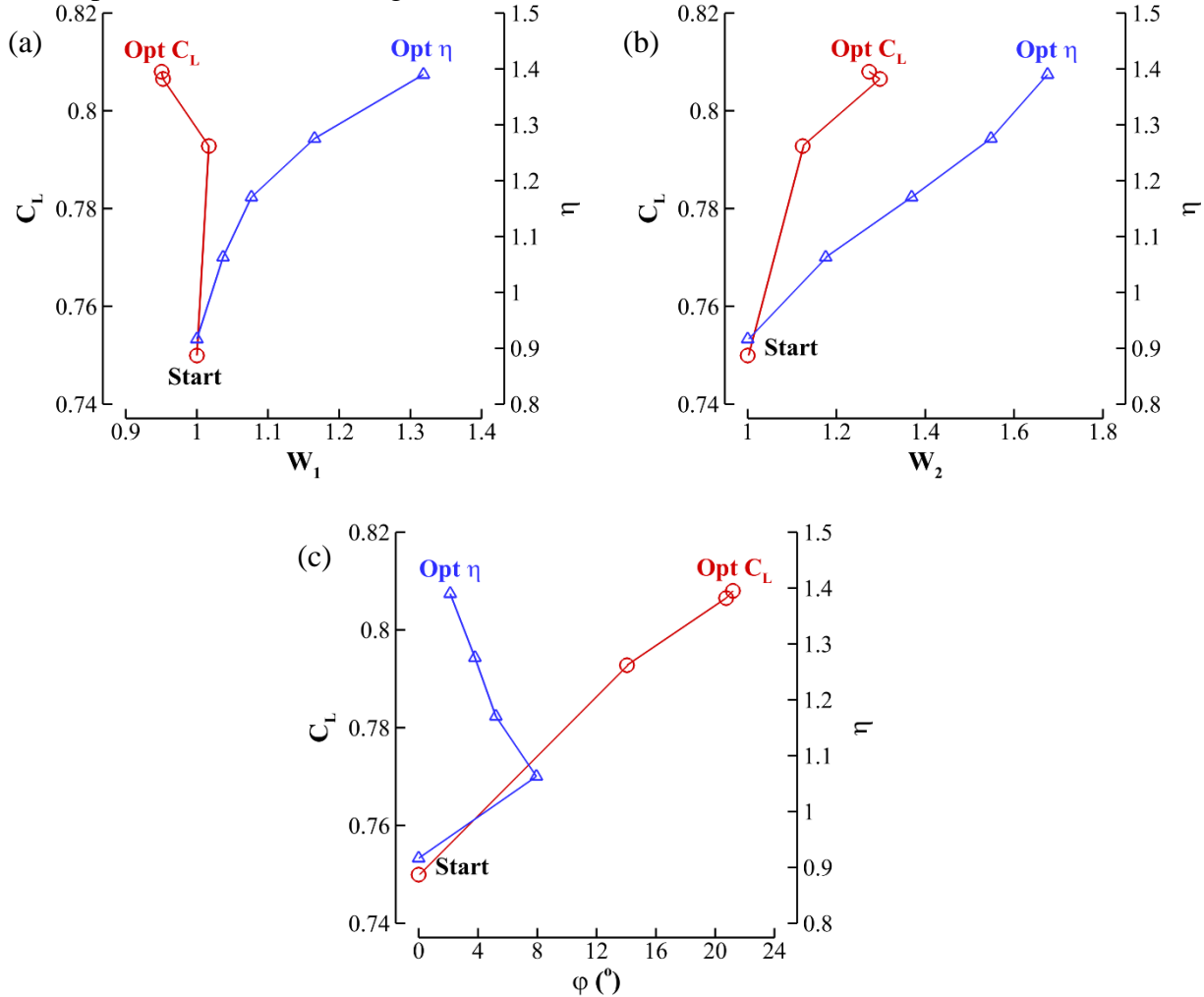


Figure 27. Convergence history for design variables (a) W_1 , (b) W_2 , and (c) φ of the two optimization cases.

Figure 27 shows the time histories of aerodynamic performance of the two optimization cases along with the case of low dimensional model Mode 1+2 for comparison. We can see that the case Opt C_L shows largest amplitude of the lift production during the downstroke among the three cases, while the case Opt η presents lowest of that. During the upstroke, the case Opt η shows largest amplitude of the lift production among the three cases, while the case Mode 1+2

presents lowest of that. For the power consumption, the case Opt η shows the lowest power consumption.

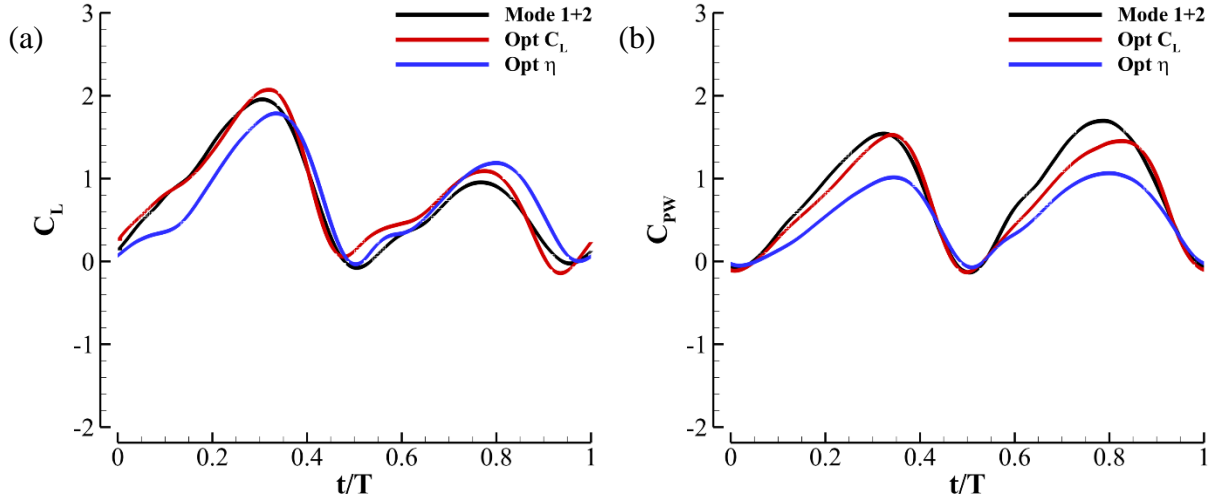


Figure 28. Comparison of the time course of aerodynamic performance of Mode 1+2 and optimized wing gaits. (a) Lift; (b) power.

Table 3 lists the cycle averaged aerodynamic performance for the two optimum cases and the case Mode 1+2. Comparing to the case Mode 1+2, the thrust production of the Opt C_L case is increased by 7.7%, and the propulsive efficiency of the Opt η case is increased by 51.6%. The SSVD modes can greatly improve the aerodynamic performance of the flapping wing, especially for the lift efficiency.

Table 3. Cycle averaged hydrodynamic performance of Mode 1+2 and optimized wing gaits.

Cases	$\overline{C_L}$	$\overline{C_{pw}}$	η
Mode 1+2	0.750	0.818	0.917
Opt C_L	0.808	0.730	1.107
Opt η	0.738	0.531	1.390

Figure 29 shows the wake structure at the $t/T=0.27$ (near the mid downstroke) and $t/T=0.73$ (near the mid upstroke) of the three cases. We can see that the general wake structures are similar for all the cases. However, the case Opt C_L shows the strongest LEV and case Opt η shows the weakest wing tip vortex.

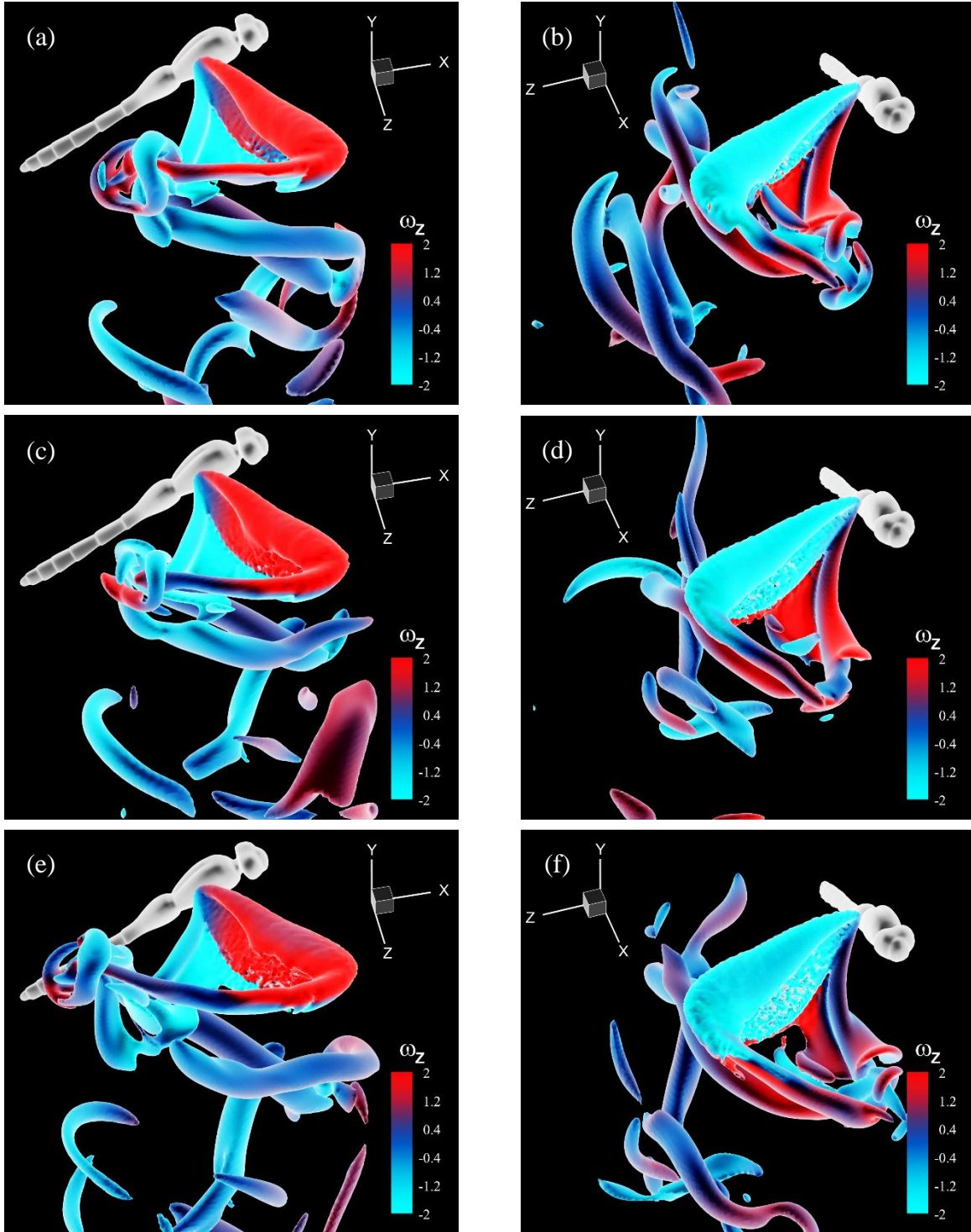


Figure 29. Wake structures for the (a) Mode 1+2, (c) Opt C_L , (e) Opt η at $t/T=0.27$; wake structures for the (b) Mode 1+2, (d) Opt C_L , (f) Opt η at $t/T=0.73$.

Concluding Remarks:

In this work, we have investigated the optimal configurations of dominant SSVD modes on aerodynamic performance for the dragonfly wing. The optimized low dimensional wing models, which can beyond biological levels of aerodynamic performance, are obtained. The associated flow mechanisms are found to be the improved LEV strength and the reduced TV strength.

3 Adjoint Optimization

The mechanism of flapping-wing aerodynamics provides an efficient way to generate necessary lift and thrust and is the most common way of flying adopted by birds and insects. In comparison to other flying mechanisms used by nature's flyers and artificial flying machines, flapping shows many attractive characteristics such as agility, hovering capability, efficiency at low Reynolds number, etc. Although some understanding is achievable through carefully designed numerical simulations [[36] Dong, H., Mittal, R. & Najjar, F. 2006 Wake topology and hydrodynamic performance of low aspect-ratio flapping foils. *J. Fluid Mech.* 566, 309–343.

-40], the problem's large parametric space prevents further physical understanding and optimization through a direct parametric study.

To achieve an understanding of all the control parameters, one often chooses to reduce the complexity of the physical model and/or the size of parametric space. Based on a quasi-steady model with 11 control parameters, Berman & Wang [41] were able to use a hybrid algorithm of the genetic method and simplex method to minimize the power consumption of insect flights. Ghommam et al. [42] used an unsteady vortex-lattice method and a deterministic global optimization algorithm for the optimization of flapping wings in forward flight with active morphing, where only 4–8 parameters were considered. Milano & Gharib [43] applied a genetic algorithm in an experimental setting to maximize the average lift from a flapping flat plate by limiting the number of control parameters to only 4. Trizila et al. [44] has used a combined approach with numerical simulation and surrogate modelling to explore a three-parameter design space for a three-dimensional plate in hovering motion. Building a map of the entire design space is useful for some problems but may not be necessary for others. On the other hand, the computational cost was still high even with a surrogate model and prevents the study from including more parameters, and the accuracy was limited by the surrogate model. There have also been efforts to use gradient-based methods for optimization. Tuncer & Kaya [45] and Culbreth, Allaneau & Jameson [46] used a gradient-based method to optimize the flapping-wing motion for better thrust and efficiency. They used direct numerical simulation for each set of control parameters and then computed the gradient of the cost function subject to the perturbation of parameters directly by finite difference. Since all parameters were evaluated individually and required their own simulation, the process became extremely expensive, and the former work was limited to 4 parameters and the latter included cases of from 1 to 11 parameters.

Different from the above works, an adjoint-based method is capable of obtaining the gradient information simultaneously for an arbitrary number of input parameters by one single computation in the adjoint space. Consequently, the total computational cost to obtain the sensitivity of a cost function to all control parameters is independent of the number of control parameters. Thus an adjoint-based method is suitable for the sensitivity analysis and optimization

of problems with a large input space but a small output space, such as the study of kinematics and deformation of flexible flapping wings. Depending on the order of applying the discretization and adjoint formulation, there are two types of adjoint approaches: the continuous approach [47,48] and the discrete approach [49,50]. Nadarajah & Jameson [51] and Collis et al. [52] have discussed the pros and cons of the two approaches. In the current work, we take the continuous approach for its simplicity and clarity in the governing equation for adjoint space, which has mathematical terms which may be interpreted as representing the generation, convection and dissipation of adjoint variables [53]. However, use of the continuous adjoint approach on flapping wings has been scarce because of the difficulty in defining the perturbation at a moving or deforming boundary [54]. In their work of applying an adjoint-based method to obtain the gradient information for the shape optimization of a plunging airfoil, Nadarajah & Jameson [55] used a mapping function to transfer the physical domain with a moving boundary to a computational domain with a fixed boundary so that traditional adjoint-based methods for a fixed domain can be directly applied (and the trouble relating to the moving boundary is avoided). Although the idea was straightforward, the mapping function increased considerably the complexity of the formulation even for their simple case where only the shape (as a steady function) of a rigid flapping airfoil was optimized. In other words, Nadarajah and Jameson were only able to optimize the steady part of an unsteady mapping function. When the moving trajectory and dynamics morphing (as an unsteady function) need to be optimized for a flapping wing, the complexity reaches a much higher level and yields the mapping-function approach infeasible. To deal with the increased complexity introduced by an unsteady morphing domain, we choose to apply non-cylindrical calculus [54,56] to derive adjoint equations directly in a morphing domain and to optimize the moving boundary in its original space without using a mapping function. The advantage of choosing non-cylindrical calculus over the unsteady mapping function has been demonstrated by Protas & Liao [56] with a comparison of the two approaches in deriving the adjoint equation for a one-dimensional heat equation with a moving boundary.

Using a continuous adjoint approach to handle the large parametric space and non-cylindrical calculus to handle the moving boundary, we can study the optimal moving trajectory and arbitrary deformation of a flapping wing. The optimal solutions of different configurations (a two-dimensional rigid flapping plate, a two-dimensional flexible flapping plate, a three-dimensional rigid flapping plate and a three-dimensional flexible flapping plate) for different control goals (thrust performance, propulsive efficiency and lift performance in hovering) provide a unique opportunity to understand the flapping-wing mechanism and the role of flexibility through a detailed comparison of optimal and non-optimal controls, corresponding flow fields and other aerodynamic performance indicators.

3.1 Governing equations for adjoint optimization

The basic derivation and notation of the continuous adjoint equations are similar to those used by Bewley et al. [47] and Wei & Freund [48], although those works dealt only with problems with a fixed domain. The inclusion of non-cylindrical calculus to formulate the adjoint equations with a morphing domain or moving boundary has been suggested by Moubachir & Zolesio [54] within a mathematical framework only and later by Protas & Liao [56] with numerical implementation for simple problems (e.g. the one-dimensional heat equation). We followed the same idea and extended its application to work for the Navier–Stokes equations.

1) Governing equation and cost function

Though the approach is not limited to a particular shape or motion, for the convenience of discussion, we consider a scenario where a plate is plunging and/or pitching with a prescribed velocity $\mathbf{V}(t)$. The flow dynamics is described by the incompressible Navier–Stokes equations,

$$\begin{cases} N(\mathbf{q}) = F & \text{in } \Omega, \\ \mathbf{u} = \mathbf{V} & \text{on } S, \\ \mathbf{u}|_{t=0} = \mathbf{u}_0 & \text{in } \Omega, \end{cases} \quad (14)$$

where Ω denotes the fluid domain, S denotes the solid boundary, the primary variable $\mathbf{q}=[\mathbf{u}, p]$ for pressure and velocity, the operator

$$N(\mathbf{q}) = \begin{bmatrix} \frac{\partial u_i}{\partial x_i} \\ \frac{\partial u_i}{\partial t} + \frac{\partial (u_i u_j)}{\partial x_j} - \nu \frac{\partial^2 u_i}{\partial x_j^2} + \frac{\partial p}{\partial x_i} \end{bmatrix}, \quad F = 0,$$

For demonstration purpose, we pick a simple cost function J , which is to minimize the overall difference between the velocity \mathbf{u} at a downstream region Ω_0 and a target velocity \mathbf{u}_{Ω_0} in that region for time period $(0, T)$:

$$J = \int_0^T \int_{\Omega} |\mathbf{u} - \mathbf{u}_{\Omega_0}|^2 d\Omega dt \quad (16)$$

This choice of cost function provides the convenience of having an obvious optimal solution: $\mathbf{u} = \mathbf{u}_{\Omega_0}$, which makes an easy validation of the approach.

2) Adjoint equation and gradient calculation

Introducing non-cylindrical calculus to define the boundary perturbation and adjoint variables $\mathbf{q}^*=[\mathbf{u}^*, p^*]$ and \mathbf{Z}^* are as Lagrange multipliers, we get derive the adjoint equation with controls for moving boundary:

$$\begin{cases} N^*(\mathbf{q})\mathbf{q}^* = F^* & \text{in } \Omega, \\ \mathbf{u}^* = 0 & \text{on } S \cup \Gamma_{\infty}, \\ \mathbf{u}^*|_{t=T} = 0 & \text{in } \Omega, \\ \frac{d\mathbf{Z}^*}{dt} + \mathbf{Z}^* \text{div}_s \mathbf{V} = (\nabla \mathbf{u})^T \bullet \boldsymbol{\sigma} \bullet \mathbf{n} & \text{on } S, \\ \mathbf{Z}^*|_{t=T} = 0 & \text{on } S, \end{cases} \quad (17)$$

where

$$N^*(\mathbf{q})\mathbf{q}^* = \begin{bmatrix} \frac{\partial u_i^*}{\partial x_i} \\ \frac{\partial u_i^*}{\partial t} + u_j \left(\frac{\partial u_i^*}{\partial x_j} + \frac{\partial u_j^*}{\partial x_i} \right) + \nu \frac{\partial^2 u_i^*}{\partial x_j^2} + \frac{\partial p^*}{\partial x_i} \end{bmatrix}, \quad F = \begin{bmatrix} 0 \\ 2(u_i - u_{\Omega_0 i}) \chi_0(\Omega_0) \end{bmatrix},$$

and

$$\chi_0 = \begin{cases} 1 & \text{in } \Omega_0 \\ 0 & \text{otherwise} \end{cases},$$

$$\sigma_{ij} = -p\delta_{ij} + \nu \left(\frac{\partial u_i^*}{\partial x_j} + \frac{\partial u_j^*}{\partial x_i} \right).$$

The above formulation defines the adjoint equations with a set of desirable boundary and initial conditions, where $t=T$ is considered the ‘initial’ time, since the adjoint system typically evolves backwards in time. With the definition of the adjoint system, the gradient is given by:

$$J' = -\int_0^T \int_S \dot{V}_i(\sigma_{ij}^* n_j + Z_i^*) ds dt, \quad (19)$$

where

$$\sigma_{ij}^* = p^* \delta_{ij} + \nu \left(\frac{\partial u_i^*}{\partial x_j} + \frac{\partial u_j^*}{\partial x_i} \right).$$

When the control is related to the change of boundary location and corresponding velocity, it provides a way to compute gradient information as a function of adjoint solutions only.

It is noticed that the first term in the gradient is for the perturbation of the boundary velocity and is the same as the term derived by the traditional approach for a fixed domain (which can still have velocity control on the boundary), and the second term is for the domain variation and is unique for a moving boundary/domain and the current approach.

3.2 Numerical algorithm

We applied different moving-boundary treatments to compute the forward (physical) flow field and the backward (adjoint) ‘flow’ field, including (i) immersed boundary method [57], (ii) arbitrary Lagrangian–Eulerian method [58] and (iii) for simple rigid cases, a moving reference frame algorithm [59]. The numerical simulations using different boundary treatments yield similar results and efficiency.

A staggered Cartesian mesh with local refinement through stretching functions is chosen for the benefit of both computational efficiency and numerical stability. We apply a second-order central difference scheme for spatial discretization, a third-order Runge–Kutta/Crank–Nicolson scheme for time advancement and a typical projection method for incompressible flow conditions [60]. With the similarity shown in the form of adjoint equations and flow equations, we apply similar numerical algorithms to solve the adjoint equations backwards in time, which leads to similar computational cost for the adjoint computation.

The gradient can be achieved after both the flow and adjoint equations are solved once. In some cases, when the control space is large and the gradient is not smooth, it may be necessary to apply a Sobolev inner product or Savitzky–Golay smoothing filters to smooth out the gradient. Meanwhile, in the main iteration to update the gradient, the Polak–Ribiere variant of the

conjugate gradient method is used; within each main iteration, Brent's method is used to determine the optimal step size along each direction and this process requires a couple of subiterations.

3.3 Validation of adjoint-based optimization solution and gradient information

To assure the accuracy of the current approach, in this section we first compare the optimal solution given by the adjoint-based algorithm to a known optimal solution, then make a further comparison between the gradient information computed by the adjoint approach and the gradient computed by a 'brute-force' finite difference approach.

Here, we consider a rigid plate plunging normally to an incoming flow. The control ϕ is the plunging velocity at each individual time moment. We pick the same cost function as discussed in section 3.1 for easy validation.

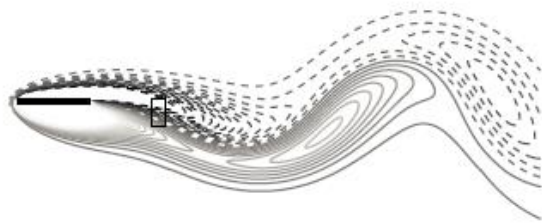


Figure 34. A typical snapshot showing the plunging plate, the flow and the observation region.

For validation, we first perform a simulation while using the target control ϕ_0 , and record the velocity field \mathbf{u}_{Ω_0} in Ω_0 as the target velocity. With some arbitrary initial control ϕ_1 , the velocity in Ω_0 is \mathbf{u} . The difference between \mathbf{u} and \mathbf{u}_{Ω_0} , as indicated by the cost function, should drive the control to match ϕ_0 if the optimization algorithm works.

Figure 35 shows the performance of the optimization algorithm by: (i) checking the change of the cost function and the gradient norm (to show the local slope of the control space) with the number of iterations; (ii) a direct comparison of the control functions (the initial ϕ_1 , the target ϕ_0 and the optimal ϕ_p). The cost function value is reduced by an order in only 2 main iterations (with several line-minimization steps for each main iteration) and by an order of 10^3 in 12 main iterations; the local gradient norm is also reduced by an order of 10^2 and reaches a 'flat spot' in 12 main iterations. At the same time, the control is changed from the initial ϕ_1 to the optimal ϕ_p . As we can expect from the reduction of the cost function, the optimal control matches very well with the target control until approximately $t=8$. The control cannot be improved much after $t=8$ because of the information delay due to the distance between the observation region Ω_0 , where the cost function is defined, and the plate, where the control is applied. The travelling time between these two points would require the simulation and the cost function to include future events at $t > 10$ in Ω_0 for optimization of the plate velocity in the time period $8 < t < 10$.

To further confirm the accuracy of the gradient (and the associated efficiency for the optimization), we validate the gradient information itself by a comparison between the gradient obtained by the adjoint approach and the gradient computed directly by a finite difference approach. The finite difference approach perturbs the control with a small value at each time moment individually and calculates the gradient directly. Although the direct approach is straightforward and considered accurate, its computational cost is proportional to the number of control parameters. Figure 36 then compares the gradients computed by the adjoint method with

the ones computed by the finite difference method, which shows good accuracy with extraordinary time saving.

To test the sensitivity of the algorithm to initial values and verify its independence of a particular function format, we run the same test with the same target control but with a very different initial control. As it is shown in figure 37, the same convergence rate is observed, and the same optimal solution is reached (for the controllable time region).

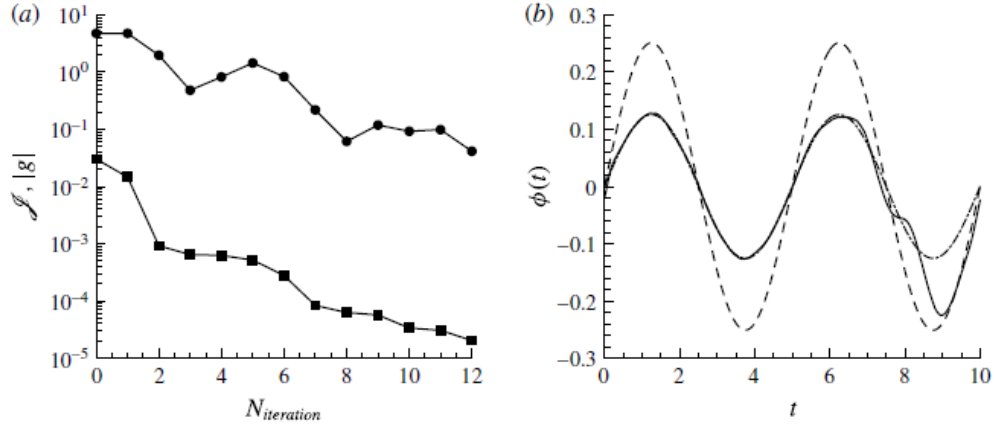


Figure 35. Adjoint-based optimization for the plunging velocity: (a) change of the cost function J and the gradient norm $|g|$ with the number of iterations; (b) comparison of the initial control ϕ_1 (---), the target control ϕ_0 (-·-) and the optimal control ϕ_p (—).

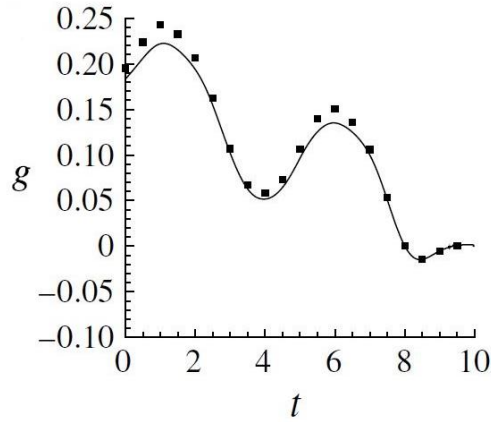


Figure 36. Comparison of the gradient g between the values computed by the adjoint method (line) and the finite difference approach through direct perturbation (square).

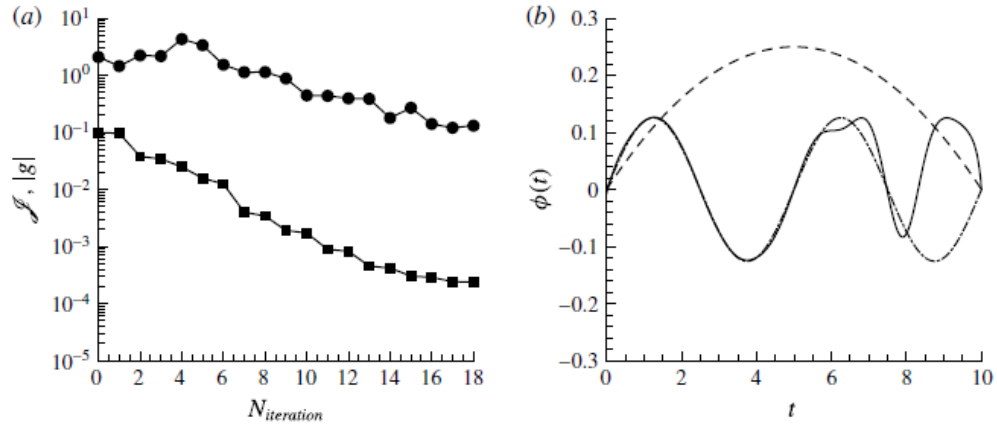


Figure 37. Adjoint-based optimization for the plunging velocity with a different initial control.

3.4 Applications to optimize the kinematics and deformation of flapping wings

In this section, the adjoint-based algorithm is applied to three cases: (i) a rigid plate in combined plunging and pitching motion with an incoming flow; (ii) a flexible plate in plunging, pitching and prescribed deformation with an incoming flow; (iii) a three dimensional (rigid or flexible) plate in hovering motion. For the first two cases, the control goals are drag reduction (i.e. thrust enhancement) and propulsive efficiency improvement; the control parameters include the phase delay between the plunging and pitching (for the rigid plate) and the phase delay and amplitude of the pitching motion and the first two eigenmodes (for the flexible plate). For the last case, the control goal is lift increase; the control parameters include the translational amplitude, the amplitude and phase delay of the rotational motion and (for the flexible plate) the amplitude and phase delay of the first eigenmode in chordwise bending.

1) Optimization of a rigid plunging and pitching plate

Anderson et al. [61] suggested the critical role of the phase delay between the pitching and the plunging motion in thrust production and propulsive efficiency, therefore, it is chosen to be the control parameter for drag reduction. The phase delay is optimized in two steps. First, we consider the phase delay to be a constant in time and search for its optimal value. Second, after the optimal constant is found, we use this value as an initial condition to optimize the phase delay further by allowing its variation in time. The two-step strategy brings the control to a good neighbourhood in a simple control space (with a constant phase delay) before it becomes a more complex control space (with a time-varying phase delay).

For the constant phase delay, we start with an arbitrary initial value $\varphi_1 = 30^\circ$. It only takes 2 iterations to reach the optimal value $\varphi_p = -77.3^\circ$. The corresponding drag coefficients, used as the cost function, is reduced from 0.120 to -0.198. For the time-varying phase delay, the initial value is chosen to be the optimal constant phase delay. The optimization algorithm reduces the drag further by 53% from -0.198 to -0.303 (figure 38).

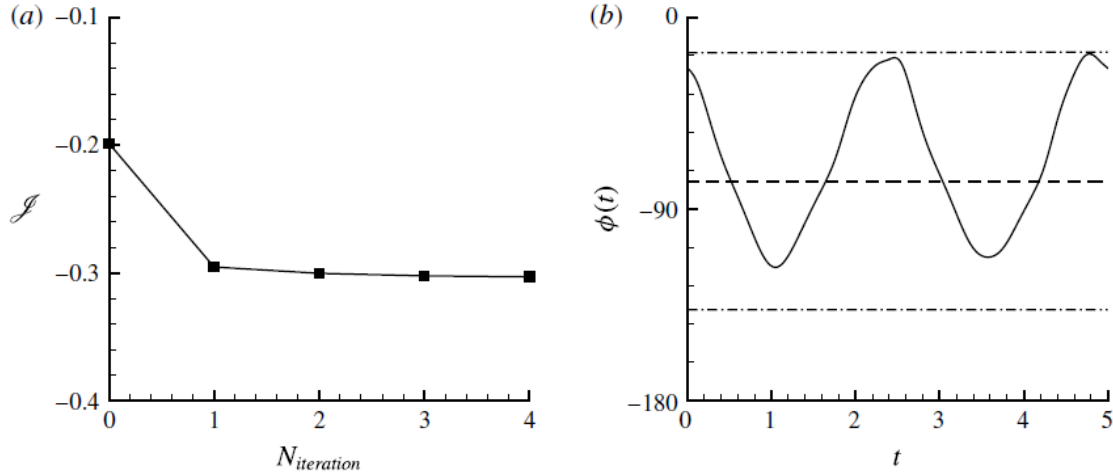


Figure 38. Optimization for the drag reduction of a rigid flapping plate: (a) the cost function for drag reduction versus the number of iterations; (b) the optimal constant control (---) and the optimal time-varying control (—), with dash-dot lines representing the constraints.

Figure 39 shows leading-edge vortex is moved from the backside of the plate to the front side. The new location of leading-edge vortex produces a low-pressure region in front of the plate which generates a large thrust force in both the upstroke and the downstroke.

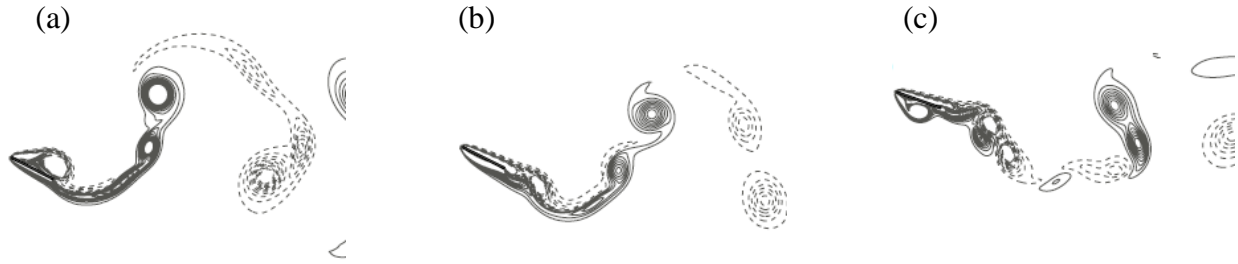


Figure 39. The vortex structures of a flapping plate with (a) the initial time constant, (b) optimal the time-constant and (c) the optimal time-varying phase delay during the upstroke.

Further analysis of the optimal control indicates that the strategy of adjusting the phase delay for thrust performance works to increase the angle of attack magnitude when the plunging speed is large to focus on the enhancement of lift-induced thrust, and works to decrease the angle of attack magnitude when the plunging speed is small to focus on the reduction of viscous drag. Meanwhile the signs for the angle of attack and the plunging velocity are kept opposite to always generate positive lift-based thrust.

When propulsive efficiency is considered, the optimization result shows that the reduction of viscous drag takes a more dominant role because of its impact on overall power consumption. The mechanism to increase power output generally works against the mechanism to reduce the total power consumption, keeping the viscous drag in check becomes the key to finding a balance between the two mechanisms for optimization.

2) Optimization of a flapping flexible plate

In this section, flexibility is added to the flapping plate, and the analysis of its aerodynamic effect is undertaken via a comparison of the optimal and non-optimal solutions.

The flexible flapping plate has a combined motion with plunging, pitching and deformation, which uses eigenmodes of a cantilevered Euler–Bernoulli beam as basis functions. The control for a flexible flapping plate is then defined by

$$\phi = \{a_0, \varphi_0, \dots, a_n, \varphi_n\}$$

where a_0, φ_0 are the amplitude and phase delay of the rigid body pitching motion, and a_n, φ_n ($n > 0$) are the amplitude and phase delay of each eigenmodes for deformation with n representing the levels of flexibility.

It is shown in table 4 and 5 that the adjoint-based optimization provides solutions for all cases to change from drag to thrust (and to larger thrust). The comparison between the rigid plate (case 1) and the flexible plates (case 2 and 3) shows significant contribution from the flexibility to the thrust improvement. At Reynolds number 300 (Group I), the optimal flexible plate (case 3) provides 111% more thrust than the rigid plate (case 1); at lower Reynolds number 100 (Group II), the impact is even more dramatic with 1069% more thrust from the rigid plate (case 1) to the flexible plate (case 3). For both Reynolds numbers, a higher level of flexibility (case 3, with 2 eigenmodes) provides more thrust than a lower level of flexibility (case 2, with 1 eigenmode). It is worth noting that the thrust brought in by more flexibility comes with some small cost of efficiency, since the propulsive efficiency is not part of the cost function at this moment.

The current study also shows that flexibility helps to reduce the sensitivity of the propulsion performance to the Reynolds number. For a rigid plate ($n=0$), the optimal thrust is reduced by 86.5% from 0.26 to 0.035 when the Reynolds number changes from 300 to 100; for a flexible plate ($n=2$), the optimal thrust is only reduced by 25.5% from 0.549 to 0.409. It suggests that flexibility helps to maintain the aerodynamic performance in complex environment with variable Reynolds number (e.g. flow with gust), and flexibility also plays a more significant role in lower Reynolds number region such as flapping-wing flight of insects.

For detailed comparison, figure 40 shows the history of drag forces for the optimal rigid plate (case 1), the optimal plate with small deformation (case 2), the optimal plate with large deformation (case 3) and the reference rigid plate (case 4, by removing the flexibility directly from case 3) for $Re=300$ (Group I). Among the half-cycle, the one with small deformation (case 2) reduces the drag by a small amount near $t=0$ and $t=1.5$; the one with large deformation (case 3) reduces the drag by a large amount near $t=0$ with a slight increase near $t=1$; the reference (case 4) keeps the same or even better drag reduction at $t=0$ but cannot maintain the same saving later, instead it adds large drag for $1 < t < 2$.

Figure 41 shows visually the flapping kinematics, deformation and vortex structures for better understanding of the control mechanism. Flexibility, especially large deformation, allows the plate to have a large angle of attack and hold the leading-edge vortex to the front for the benefit of lift-induced thrust, while the overall profile stays small (by deformation) to avoid an increase in viscous drag. It is obvious that the reference case 4, which keeps the same pitching (i.e. angle of attack) at the leading edge but removes all the deformations, has the same benefit from the lift-induced thrust (near $t=0$) but adds a huge amount of viscous drag later.

Table 4. Optimization results for drag reduction with different flexibility at $Re=300$: cases 0 has the initial control; cases 1, 2 and 3 have the optimal controls with different levels of flexibility; case 4 is a reference case, which removes all flexibility terms from case 3 and keeps the rigid plunging and pitching motion the same. η is the propulsion efficiency.

Group	Cases	n	C_d	η
I	0	0	0.138	-0.0373
	1	0	-0.260	0.184
	2	1	-0.376	0.296
	3	2	-0.549	0.273
	4	0	0.696	-0.141

Table 5. Optimization results for drag reduction with different flexibility at Re=100.

Group	Cases	n	C_d	η
II	0	0	0.165	-0.473
	1	0	-0.035	0.0194
	2	1	-0.177	0.0892
	3	2	-0.409	0.116

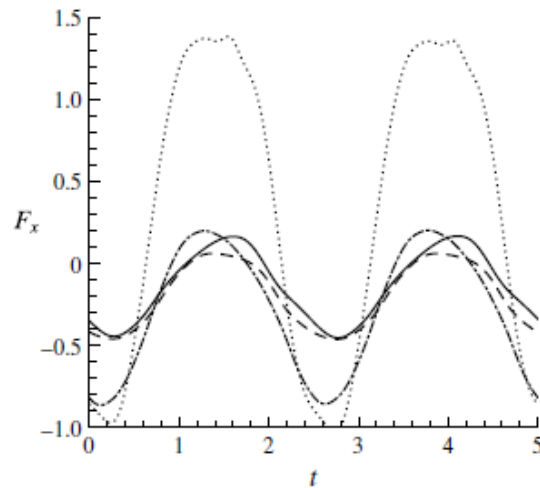


Figure 40. The history of drag forces in one period for case 1 (—), case 2 (---), case 3 (— · —) and case 4 (·····) of Group I.

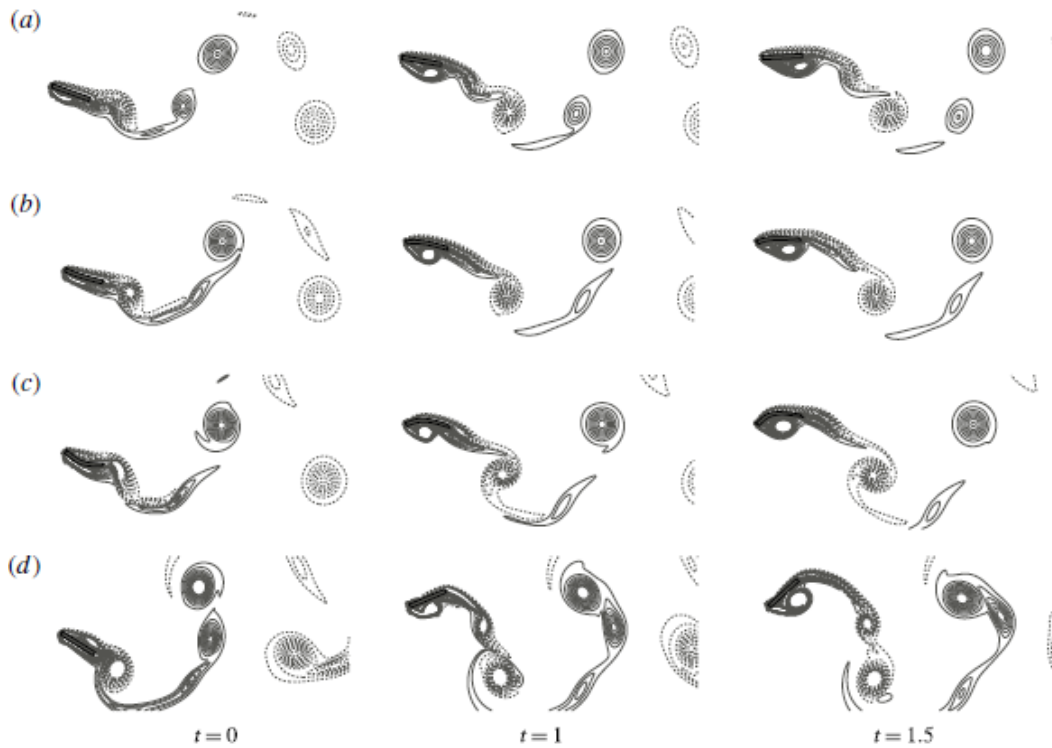


Figure 41. Comparison of kinematics, deformation and vortex structures of (a) the rigid plate (case 1), (b) the plate with small deformation (case 2), (c) the plate with large deformation (case 3) and (d) the reference (case 4), with $Re=300$ (Group I), at $t=0, 1$ and 1.5 .

Adjoint-based optimization also improves the propulsive efficiency substantially (table 6). The optimal solution shows that plate tries to blend into a streamline shape to reduce the viscous drag. Meanwhile holding a large leading-edge vortex is no longer an option with its cost on viscous drag. Same as that in drag reduction, flexibility also largely reduces the sensitivity of propulsive efficiency to Reynolds number and allows a flapping wing at low Reynolds number to enjoy the high aerodynamic performance existing in the higher Reynolds number regime.

Table 6. Optimization results for propulsive efficiency with different flexibility at $Re=300$.

Group	Cases	n	C_d	η
III	0	0	0.138	-0.0373
	1	0	-0.223	0.247
	2	1	-0.307	0.373
	3	2	-0.347	0.377

3) Optimization of a three-dimensional plate in hovering motion

In this section, we extend the study from a two-dimensional plate to a three-dimensional plate. We choose the same rigid plate in hovering motion, which has been studied extensively by Trizila et al. [44], as our base case. With initial numerical simulations combined with surrogate modelling, Trizila et al. [44] achieved the complete map of a three-parameter design space including: the amplitude of translational motion x_0 , the amplitude θ_α and the phase delay of rotational motion φ . Such a space exploration is important for some cases. However, an adjoint-based optimization could be much more efficient if optimization is the major concern and the result is more accurate without involving a surrogate model.

Table 7 shows respectively the initial control and its optimal value after 4 main iterations. The lift coefficient is improved from 0.338 to 0.620 by 83.4 %. A closer comparison shows that our optimal values match well with the high-lift region shown in the contour map provided by the design space exploration through surrogate modelling in Trizila et al. [44].

Table 7. Comparison of the initial and the optimal controls and the resulting lift coefficients for a rigid hovering plate.

Control	x_0	θ_α	φ	C_l
Initial	1.5	60°	90°	0.338
Optimal	1.0	45°	120°	0.620

Figures 42 compares the time history of lift coefficients with the initial and the optimal controls. Compared to the initial control, the plate with the optimal control has a larger angle of attack at $t=0$. This generates a stronger leading-edge vortex (figure 43), which causes large pressure difference in upper and lower surface of the plate (figure 44) and produces larger lift. At $t=0.2$, in the case with the initial control, the vortex pair generates a momentum on the plate's upper surface (figure 43), therefore it produces downward force (figure 44). On the other hand, the plate with the optimal control has an advanced rotation. The momentum induced by the vortex pair acts on the plate's lower surface, thus generating lift instead. These results suggest that, in hovering flight, both the plunging/pitching and the wake capture are important for lift generation. The timing of the plate interacting with the wake is closely related to the phase delay. The vortex structures depicted in figure 45 by an isosurface of Q criterion clearly show much stronger downwash from the optimal motion for the increase of lift performance.

When chord-wise deformation is considered during the optimization, the lift coefficient is pushed from 0.62 to 0.88 for another 42% increase. The flexibility is able to push the lift coefficient higher by 'cupping' more fluid on the lower surface and deforming to larger vertical projection profile which lead to an even stronger downwash as well as larger pressure difference between the upper and lower surfaces of the plate, both for lift benefit.

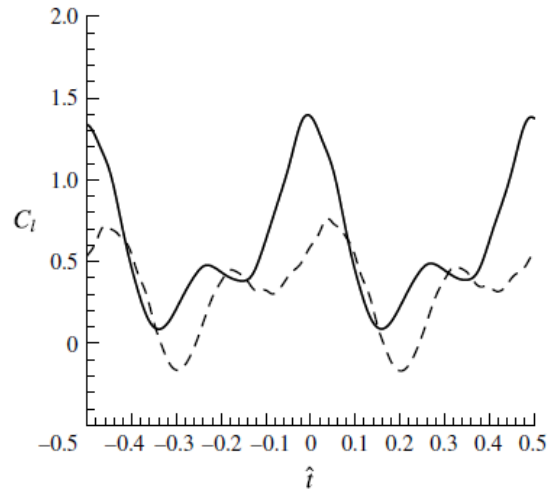


Figure 42. The time history of the lift coefficients for a rigid hovering plate with the initial control (---) and the optimal control (—).

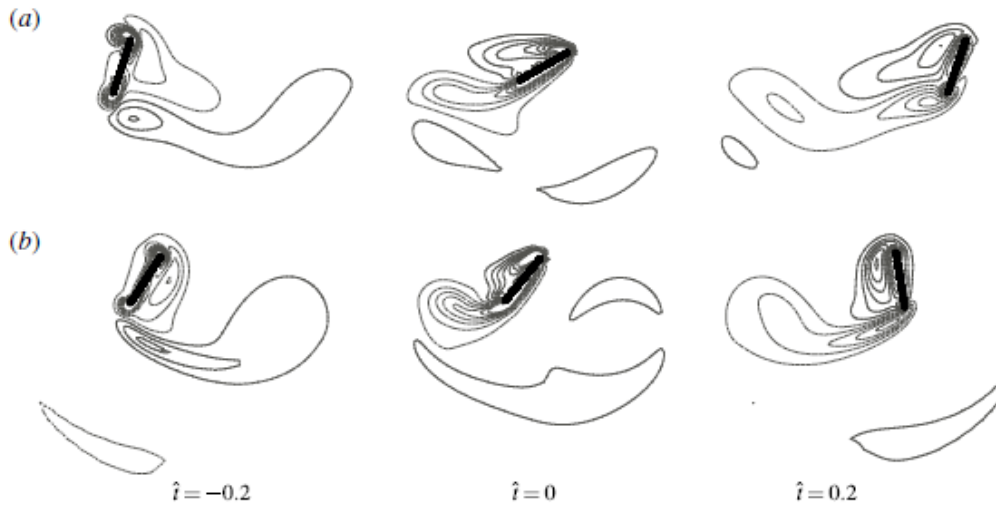


Figure 43. The z-component of vorticity at the middle plane for a rigid hovering plate with (a) the initial control and (b) the optimal control at different time moments.

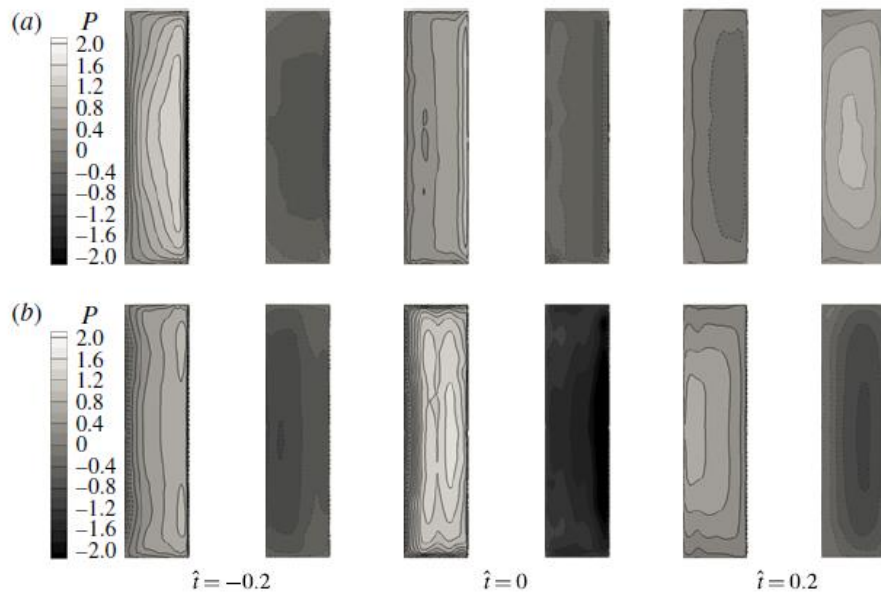


Figure 44. The pressure distribution of a rigid hovering plate with (a) the initial control and (b) the optimized control on the lower (left) and upper (right) surfaces at different time moments.

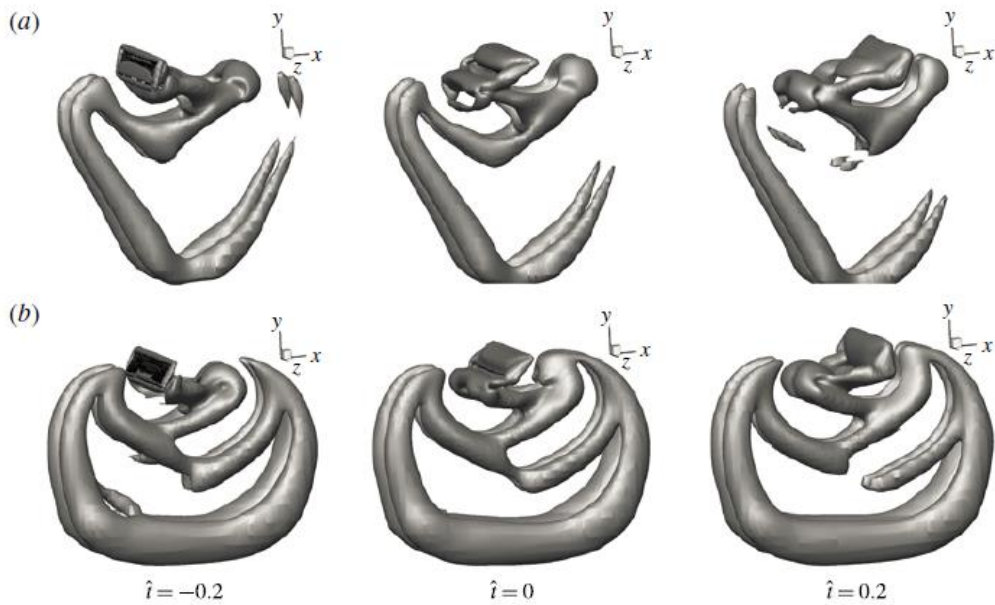


Figure 45. The vortex structures of a rigid hovering plate with (a) the initial control and (b) the optimal control at different time moments.

4 References

- [1] C. Koehler, Z.X. Liang, Z. Gaston, H. Wan, H.B. Dong, 3D reconstruction and analysis of wing deformation in free-flying dragonflies, *J Exp Biol*, 215 (2012) 3018-3027.
- [2] E. Catmull, J. Clark, Recursively Generated B-Spline Surfaces on Arbitrary Topological Meshes, *Comput Aided Design*, 10 (1978) 350-355.
- [3] R.R. Harbig, J. Sheridan, M.C. Thompson, Reynolds number and aspect ratio effects on the leading-edge vortex for rotating insect wing planforms, *J Fluid Mech*, 717 (2013) 166-192.
- [4] R.H. Pletcher, J.C. Tannehill, D. Anderson, *Computational fluid mechanics and heat transfer*, CRC Press 2012.
- [5] M. Bozkurtas, H. Dong, V. Seshadri, R. Mittal, F. Najjar, Towards numerical simulation of flapping foils on fixed Cartesian grids, *AIAA Paper*, 81 (2005) 2005.
- [6] G. Schneider, M. Zedan, A modified strongly implicit procedure for the numerical solution of field problems, *Numerical Heat Transfer*, 4 (1981) 1-19.
- [7] J. Ruge, K. Stüben, Algebraic multigrid, *Multigrid methods*, 3 (1987) 73-130.
- [8] K. Stuben, A review of algebraic multigrid, *J Comput Appl Math*, 128 (2001) 281-309.
- [9] D.J. Mavriplis, V. Venkatakrishnan, A 3D agglomeration multigrid solver for the Reynolds-averaged-Navier-Stokes equations on unstructured meshes, *Int J Numer Meth Fl*, 23 (1996) 527-544.
- [10] T. Ye, R. Mittal, H.S. Udaykumar, W. Shyy, An accurate Cartesian grid method for viscous incompressible flows with complex immersed boundaries, *J Comput Phys*, 156 (1999) 209-240.
- [11] H.S. Udaykumar, R. Mittal, P. Rampunggoon, A. Khanna, A sharp interface cartesian grid method for simulating flows with complex moving boundaries, *J Comput Phys*, 174 (2001) 345-380.
- [12] R. Mittal, H. Dong, M. Bozkurtas, F.M. Najjar, A. Vargas, A. von Loebbecke, A versatile sharp interface immersed boundary method for incompressible flows with complex boundaries, *J Comput Phys*, 227 (2008) 4825-4852.
- [13] J.L. Song, H.X. Luo, T.L. Hedrick, Three-dimensional flow and lift characteristics of a hovering ruby-throated hummingbird, *J R Soc Interface*, 11 (2014).
- [14] D.R. Warrick, B.W. Tobalske, D.R. Powers, Lift production in the hovering hummingbird, *P Roy Soc B-Biol Sci*, 276 (2009) 3747-3752.
- [15] D.R. Warrick, B.W. Tobalske, D.R. Powers, Aerodynamics of the hovering hummingbird, *Nature*, 435 (2005) 1094-1097.
- [16] M.H. Dickinson, F.-O. Lehmann, S.P. Sane, Wing rotation and the aerodynamic basis of insect flight, *Science*, 284 (1999) 1954-1960.
- [17] C. Ellington, The aerodynamics of hovering insect flight. IV. aerodynamic mechanisms, *Philosophical Transactions of the Royal Society of London. B, Biological Sciences*, 305 (1984) 79-113.
- [18] C. Ellington, C. van Den Berg, A.P. Willmott, A.L.R. Thomas, Leading-edge vortices in insect flight, *Nature*, 384 (1996) 625-630.
- [19] D. Lentink, M.H. Dickinson, Rotational accelerations stabilize leading edge vortices on revolving fly wings, *Journal of Experimental Biology*, 212 (2009) 2705-2719.
- [20] H. Aono, F. Liang, H. Liu, Near- and far-field aerodynamics in insect hovering flight: an integrated computational study, *J Exp Biol*, 211 (2008) 239-257.
- [21] R.J. Bomphrey, G.K. Taylor, A.L.R. Thomas, Smoke visualization of free-flying bumblebees indicates independent leading-edge vortices on each wing pair, *Experiments in Fluids*, 46 (2009) 811-821.

- [22] G. Liu, H. Dong, C. Li, Vortex dynamics and new lift enhancement mechanism of wing–body interaction in insect forward flight, *Journal of Fluid Mechanics*, 795 (2016) 634–651.
- [23] L. Zheng, T.L. Hedrick, R. Mittal, Time-varying wing-twist improves aerodynamic efficiency of forward flight in butterflies, *PloS one*, 8 (2013) e53060.
- [24] T.Q. Le, T. Van Truong, S.H. Park, T.Q. Truong, J.H. Ko, H.C. Park, D. Byun, Improvement of the aerodynamic performance by wing flexibility and elytra–hind wing interaction of a beetle during forward flight, *Journal of The Royal Society Interface*, 10 (2013) 20130312.
- [25] J. Young, S.M. Walker, R.J. Bomphrey, G.K. Taylor, A.L.R. Thomas, Details of Insect Wing Design and Deformation Enhance Aerodynamic Function and Flight Efficiency, *Science*, 325 (2009) 1549–1552.
- [26] C. Li, Computational Investigation of Vortex Dynamics and Aerodynamic Performance in Flapping Propulsion, University of Virginia, 2016.
- [27] J.M. Wakeling, Dragonfly aerodynamics and unsteady mechanisms: a review, *Odonatologica*, 22 (1993) 319.
- [28] D.E. Alexander, Wind tunnel studies of turns by flying dragonflies, *Journal of Experimental Biology*, 122 (1986) 81–98.
- [29] G. Ruppell, Kinematic Analysis of Symmetrical Flight Maneuvers of Odonata, *Journal of Experimental Biology*, 144 (1989) 13–42.
- [30] H. Wang, L. Zeng, H. Liu, C. Yin, Measuring wing kinematics, flight trajectory and body attitude during forward flight and turning maneuvers in dragonflies, *J Exp Biol*, 206 (2003) 745–757.
- [31] Y.C. Liang, H.P. Lee, S.P. Lim, W.Z. Lin, K.H. Lee, C.G. Wu, Proper orthogonal decomposition and its applications - Part I: Theory, *J Sound Vib*, 252 (2002) 527–544.
- [32] R. Urtasun, P. Fua, P. Ghardon, D. Thalmann, Mahalanobis motion generation, *Tech Rep*, (2004).
- [33] M. Bozkurttas, R. Mittal, H. Dong, G.V. Lauder, P. Madden, Low-dimensional models and performance scaling of a highly deformable fish pectoral fin, *J Fluid Mech*, 631 (2009) 311–342.
- [34] M. Alexa, W. Muller, Representing animations by principal components, *Comput Graph Forum*, 19 (2000) C411–C418.
- [35] N.F. Troje, Decomposing biological motion: A framework for analysis and synthesis of human gait patterns, *J Vision*, 2 (2002) 371–387.
- [36] Dong, H., Mittal, R. & Najjar, F. 2006 Wake topology and hydrodynamic performance of low aspect-ratio flapping foils. *J. Fluid Mech.* 566, 309–343.
- [37] Dong, H. & Liang, Z. 2010 Effects of ipsilateral wing-wing interactions on aerodynamic performance of flapping wings. *AIAA Paper* 2010-71.
- [38] Liang, Z., Dong, H. & Wei, M. 2010 Computational analysis of hovering hummingbird flight. *AIAA Paper* 2010-555.
- [39] Yang, T., Wei, M. & Zhao, H. 2010 Numerical study of flexible flapping wing propulsion. *AIAA J.* 48 (12), 2909–2915.
- [40] Yin, B. & Luo, H. 2010 Effect of wing inertia on hovering performance of flexible flapping wings. *Phys. Fluids* 22, 111902.
- [41] Berman, G. J. & Wang, Z. J. 2007 Energy-minimizing kinematics in hovering insect flight. *J. Fluid Mech.* 582, 153–168.

- [42] Ghommem, M., Hajj, M. R., Mook, D. T., Stanford, B. K., Beran, P. S., Snyder, R. D. & Watson, L. T. 2012 Global optimization of actively morphing flapping wings. *J. Fluids Struct.* 33, 210–228.
- [43] Milano, M. & Gharib, M. 2005 Uncovering the physics of flapping flat plates with artificial evolution. *J. Fluid Mech.* 534, 403–409.
- [44] Trizila, P., Kang, C.-K., Aono, H., Shyy, W. & Visbal, M. 2011 Low-Reynolds-number aerodynamics of a flapping rigid flat plate. *AIAA J.* 49 (4), 806–823.
- [45] Tuncer, I. H. & Kaya, M. 2005 Optimization of flapping airfoils for maximum thrust and propulsive efficiency. *AIAA J.* 43 (11), 2329–2336.
- [46] Culbreth, M., Allaneau, Y. & JAMESON, A. 2011 High-fidelity optimization of flapping airfoils and wings. *AIAA Paper* 2011-3521.
- [47] Bewley, T. R., Moin, P. & Temam, R. 2001 DNS-based predictive control of turbulence: an optimal benchmark for feedback algorithms. *J. Fluid Mech.* 447, 179–225.
- [48] Wei, M. & Freund, J. B. 2006 A noise-controlled free shear flow. *J. Fluid Mech.* 546, 123–152.
- [49] Lee, B. J., Padulo, M. & Liou, M.-S. 2011 Non-sinusoidal trajectory optimization of flapping airfoil using unsteady adjoint approach. *AIAA Paper* 2011-1312.
- [50] Jones, M. & Yamaleev, N. K. 2013 Adjoint-based shape and kinematics optimization of flapping wing propulsive efficiency. *AIAA Paper* 2013-2472.
- [51] Nadarajah, S. & Jameson, A. 2000 A comparison of the continuous and discrete adjoint approach to automatic aerodynamic optimization. *AIAA Paper* 2000-667.
- [52] Collis, S. S., Ghayour, K., Heinkenschloss, M., Ulbrich, M. & Ulbrich, S. 2001 Towards adjoint-based methods for aeroacoustic control. *AIAA Paper* 2001-0821.
- [53] Wang, Q. & Gao, J. 2013 The drag-adjoint field of a circular cylinder wake at Reynolds numbers 20, 100 and 500. *J. Fluid Mech.* 730, 145–161.
- [54] Moubachir, M. & Zolesio, J.-P. 2006 *Moving Shape Analysis and Control: Applications to Fluid Structure Interactions*, Pure and Applied Mathematics, vol. 277. Chapman & Hall/CRC.
- [55] Nadarajah, S. K. & Jameson, A. 2007 Optimum shape design for unsteady flows with timeaccurate continuous and discrete adjoint method. *AIAA J.* 45 (7), 1478–1491.
- [56] Protas, B. & Liao, W. 2008 Adjoint-based optimization of pdes in moving domains. *J. Comput. Phys.* 227 (4), 2707–2723.
- [57] Mittal, R., Dong, H., Bozkurtas, M., Najjar, F., Vargas, A. & Von loebbecke, A. 2008 A versatile sharp interface immersed boundary method for incompressible flows with complex boundaries. *J. Comput. Phys.* 227 (10), 4825–4852.
- [58] Hirt, C., Amsden, A. A. & Cook, J. 1974 An arbitrary Lagrangian-Eulerian computing method for all flow speeds. *J. Comput. Phys.* 14 (3), 227–253.
- [59] Li, L., Sherwin, S. & Bearman, P. W. 2002 A moving frame of reference algorithm for fluid/structure interaction of rotating and translating bodies. *Intl J. Numer. Meth. Fluids* 38 (2), 187–206.
- [60] Xu, M., Wei, M., Yang, T. & Lee, Y. S. 2016 An embedded boundary approach for the simulation of a flexible flapping wing at different density ratio. *Eur. J. Mech. (B/Fluids)* 55, 146–156.
- [61] Andersen, A., Pesavento, U. & Wang, Z. 2005 Unsteady aerodynamics of fluttering and tumbling plates. *J. Fluid Mech.* 541, 65–90.

5 Performance Metric

5.1 Peer-reviewed Journal and Conference Papers

1. S. Zeyghami, H. Dong, Torsional wing flexibility enhances maneuverability in flapping flight, *Physical Rev. E*. 2016, under review.
2. C. Li, H. Dong, Three-dimensional wake topology and propulsive performance of low-aspect-ratio pitching-rolling plates, *Physics of fluids*, 28, 071901, 2016.
3. G. Liu, H. Dong, C. Li, Vortex dynamics and new lift enhancement mechanism of wing-body interaction in insect forward flight, *Journal of Fluid Mechanics*, 795, 634-651, 2016.
4. S. Zeyghami, N. Babu, H. Dong, Cicada (*Tibicen linnei*) steers by force vectoring, *Theoretical and Applied Mechanics Letters*, 6, 107-111, 2016.
5. C. Li, H. Dong, and G. Liu, “Effects of a Dynamic Trailing-Edge Flap on the Aerodynamic Performance and Flow Structures in Hovering Flight”, *Journal of Fluid and Structures*, 58, 49–65, 2015.
6. Y. Ren, H. Dong, Low-dimensional Modeling and Aerodynamics of Flexible Wings in Flapping Flight, 34th AIAA Applied Aerodynamics Conference, Washington DC, Jun. 13-17, 2016, AIAA-2016-4168.
7. S. Zeyghami, A. T. Bode-Oke, H. Dong, Effect of body configuration and deformation on the dynamic stability of flapping flight, AIAA Atmospheric Flight Mechanics Conference, Washington DC, Jun. 13-17, 2016, AIAA 2016-3540.
8. C. Li, H. Dong, Quantification and Analysis of Propulsive Wake Topologies in Finite Aspect-Ratio Pitching-Rolling Plates, 46th AIAA Fluid Dynamics Conference, Washington DC, Jun. 13-17, 2016, AIAA 2016-4339.
9. C. Li, H. Dong, Z. Liang, Proper Orthogonal Decomposition Analysis of 3-D Wake Structures in a Pitching-Rolling Plate. 54th AIAA Aerospace Sciences Meeting, San Diego, California, Jan. 9- 13, 2016, AIAA-2016-2071.
10. Y. Ren, G. Liu, H. Dong, Effect of surface morphing on the wake structure and performance of pitching-rolling plates. 53rd AIAA Aerospace Sciences Meeting, AIAA 2015-1490, Kissimmee, Florida, Jan. 5-9, 2015
11. C. Li, H. Dong and Y. Ren, A Numerical Study of Flapping Plates Hinged with a Trailing-Edge Flap”, 32nd AIAA Applied Aerodynamics Conference, AIAA-2014-2049, Atlanta, Georgia, June 2014.
12. C. Li, H. Dong, and Y. Ren, “A Numerical Study of Flapping Plates Hinged with a Trailing-Edge Flap”, 32nd Aerospace Sciences Meeting, AIAA paper (to appear), Atlanta, Georgia, Jun. 16-20, 2014.
13. Y. Ren, H. Dong, Computational Optimization of Flexible Wing Aerodynamic Performance in Hover, 30th AIAA Applied Aerodynamics Conference, New Orleans, Louisiana, June 2012, AIAA-2012-3116.
14. M. Xu, and M. Wei, Using adjoint-based optimization to study kinematics and deformation of flapping wings, *J. Fluid Mech.*, Vol. 799, pp. 56–99, 2016.

15. M. Xu, M. Wei, T. Yang, and Y. S. Lee, An embedded boundary approach for the simulation of a flexible flapping wing at different density ratio, *European Journal of Mechanics – B/Fluids* Vol. 55, pp. 146–136, 2016.
16. M. Xu, M. Wei, C. Li, and H. Dong, Adjoint-based optimization of flapping plates hinged with a trailing-edge flap, *Theoretical and Applied Mechanics Letters*, Vol. 5, pp. 1–4, 2015.
17. M. Xu, M. Wei, A continuous adjoint-based approach for the optimization of wing flapping, *AIAA paper 2014-2048*, Atlanta, GA, 2014.
18. M. Xu, M. Wei, Using adjoint-based approach to study flapping wings, *AIAA paper 2013-0839*, Grapevine, TX, 2013.

5.2 Theses

1. C. Li, Computational investigation of vortex dynamics and aerodynamic performance in flapping propulsion, PhD dissertation, University of Virginia, 2016.
2. S. Zeyghami, Wing in the loop: integrating wing into the dynamics of insect flight, PhD dissertation, University of Virginia, 2015.
3. Z. Liang, “Computational Analysis of Vortex Structures in Flapping Flight”, PhD dissertation, Mechanical and Materials Engineering, PhD dissertation, Wright State University, 2013.
4. C. Li, “Unsteady Flow and Aerodynamic Effect of a Dynamic Trailing-Edge Flap in Flapping Flight”, Master thesis, Mechanical and Aerospace Engineering, University of Virginia, 2014.
5. M. Xu, “Understanding Flapping-wing Aerodynamics Through Adjoint-based Approach”, PhD dissertation, New Mexico State University, 2014.

5.3 Awards and media exposure

1. Yan Ren, Media exposure, **ScienceNews**, January 2016
2. Yan Ren, Media exposure, **New York Times**, December 2015
3. Yan Ren, **Third place** in the gallery of fluid motion at 68th Annual Meeting of APS Division of Fluid Dynamics, November, 2015
4. Haibo Dong, **AIAA Abe M. Zarem Educator Award**, November, 2015
5. Ayodeji T Bode-Oke, **AIAA Abe M. Zarem Award**, November, 2015
6. Haibo Dong, Award for outstanding contribution to the Mechanical Engineering students of UVa. May 2014
7. Mingjun Wei, NMSU Millionaire Research Award, 2014
8. Min Xu, NMSU College of Engineering Dean’s Award, 2013 - 2014
9. **The American Scholar** Vol 83, No. 2, Spring 2014 “Secrets of Dragonflies”.
10. **The UVa Magazine**, July 2013 “Flight of the Cicadas”.
11. **UVa Today**, July 30, 2013 “Engineering Team Studying Insect Flight to Build Robots”.
12. **2013 UVA president’s Report**, Discovering the Joys of Research.

5.4 Students support

Hui Wan (Postdoc), Geng Liu (Postdoc), Zongxian Liang (PhD student, Postdoc), Yan Ren (PhD student), Samane Zeyghami (PhD Student), Chengyu Li (PhD Student), Min Xu (PhD Student), Kun Jia (PhD Student).

AFOSR Deliverables Submission Survey

Response ID:6730 Data

1.

Report Type

Final Report

Primary Contact Email

Contact email if there is a problem with the report.

hd6q@virginia.edu

Primary Contact Phone Number

Contact phone number if there is a problem with the report

4342434098

Organization / Institution name

University of Virginia

Grant/Contract Title

The full title of the funded effort.

Physics-based Morphology Analysis and Adjoint Optimization of Flexible Flapping Wings

Grant/Contract Number

AFOSR assigned control number. It must begin with "FA9550" or "F49620" or "FA2386".

FA9550-12-1-0071

Principal Investigator Name

The full name of the principal investigator on the grant or contract.

Haibo Dong

Program Officer

The AFOSR Program Officer currently assigned to the award

Douglas Smith

Reporting Period Start Date

06/01/2012

Reporting Period End Date

05/31/2016

Abstract

Changes in the dynamic morphology of the wing in flapping flights directly affect the instantaneous aerodynamic forces and therefore flight behavior. The wing shape and how it moves through the flow is the primary mechanism for momentum transfer to the fluid in the flapping flights. During this project period, high-fidelity CFD simulation and adjoint analysis/optimization tool has been used to study the aerodynamic role of wing morphology models built from the previous year and their interaction in a vast parametric space including aspect ratio, direction of flexibility (chord-wise, span-wise, etc.). Aerodynamic performance has been evaluated by looking at lift production, power consumption, and efficiency. Novel tools for studying wing morphing during complicated flapping flights have been developed to understand the underlying physics of flexible wings in flying insects and birds towards the bio-inspired wing designs with superior aerodynamic performance. In this funded work, we built up a team with experts from two institutes and hope to address the following basic questions about the aerodynamics of flapping flight:

1.What are the detailed features of morphing flapping wings and how to build up high-fidelity kinematic models?

2.What is the proper way(s) to characterize the wing morphing and describe the key motion components?

DISTRIBUTION A: Distribution approved for public release.

3. What is the vortex dynamics and associated aerodynamics in morphing wing flapping flight?
4. How to design morphing wing kinematics to achieve the optimal performance of the wing beyond biology?
5. What is optimal solution for 2D and 3D rigid/flexible flapping wings, and what we can learn from these mathematically optimal solutions?

Distribution Statement

This is block 12 on the SF298 form.

Distribution A - Approved for Public Release

Explanation for Distribution Statement

If this is not approved for public release, please provide a short explanation. E.g., contains proprietary information.

SF298 Form

Please attach your [SF298](#) form. A blank SF298 can be found [here](#). Please do not password protect or secure the PDF. The maximum file size for an SF298 is 50MB.

[sf0298-AFOSR.pdf](#)

Upload the Report Document. File must be a PDF. Please do not password protect or secure the PDF. The maximum file size for the Report Document is 50MB.

[AFOSR-finalreport.pdf](#)

Upload a Report Document, if any. The maximum file size for the Report Document is 50MB.

Archival Publications (published) during reporting period:

1. C. Li, H. Dong, Three-dimensional wake topology and propulsive performance of low-aspect-ratio pitching-rolling plates, *Physics of fluids*, 28, 071901, 2016.
2. G. Liu, H. Dong, C. Li, Vortex dynamics and new lift enhancement mechanism of wing-body interaction in insect forward flight, *Journal of Fluid Mechanics*, 795, 634-651, 2016.
3. S. Zeyghami, N. Babu, H. Dong, Cicada (*Tibicen linnei*) steers by force vectoring, *Theoretical and Applied Mechanics Letters*, 6, 107-111, 2016.
4. C. Li, H. Dong, and G. Liu, "Effects of a Dynamic Trailing-Edge Flap on the Aerodynamic Performance and Flow Structures in Hovering Flight", *Journal of Fluid and Structures*, 58, 49-65, 2015.
5. Y. Ren, H. Dong, Low-dimensional Modeling and Aerodynamics of Flexible Wings in Flapping Flight, 34th AIAA Applied Aerodynamics Conference, Washington DC, Jun. 13-17, 2016, AIAA-2016-4168.
6. S. Zeyghami, A. T. Bode-Oke, H. Dong, Effect of body configuration and deformation on the dynamic stability of flapping flight, AIAA Atmospheric Flight Mechanics Conference, Washington DC, Jun. 13-17, 2016, AIAA 2016-3540.
7. C. Li, H. Dong, Quantification and Analysis of Propulsive Wake Topologies in Finite Aspect-Ratio Pitching-Rolling Plates, 46th AIAA Fluid Dynamics Conference, Washington DC, Jun. 13-17, 2016, AIAA 2016-4339.
8. C. Li, H. Dong, Z. Liang, Proper Orthogonal Decomposition Analysis of 3-D Wake Structures in a Pitching-Rolling Plate. 54th AIAA Aerospace Sciences Meeting, San Diego, California, Jan. 9- 13, 2016, AIAA-2016-2071.
9. Y. Ren, G. Liu, H. Dong, Effect of surface morphing on the wake structure and performance of pitching-rolling plates. 53rd AIAA Aerospace Sciences Meeting, AIAA 2015-1490, Kissimmee, Florida, Jan. 5-9, 2015
10. C. Li, H. Dong and Y. Ren, A Numerical Study of Flapping Plates Hinged with a Trailing-Edge Flap", 32nd AIAA Applied Aerodynamics Conference, AIAA-2014-2049, Atlanta, Georgia, June 2014.
11. C. Li, H. Dong, and Y. Ren, "A Numerical Study of Flapping Plates Hinged with a Trailing-Edge Flap", 32nd Aerospace Sciences Meeting, AIAA paper (to appear), Atlanta, Georgia, Jun. 16-20, 2014.
12. Y. Ren, H. Dong, Computational Optimization of Flexible Wing Aerodynamic Performance in Hover, 30th AIAA Applied Aerodynamics Conference, New Orleans, Louisiana, June 2012, AIAA-2012-3116.
13. M. Xu, and M. Wei, Using adjoint-based optimization to study kinematics and deformation of flapping wings, *J. Fluid Mech.*, Vol. 799, pp. 56-99, 2016.
14. M. Xu, M. Wei, T. Yang, and Y. S. Lee, An embedded boundary approach for the simulation of a flexible

DISTRIBUTION A: Distribution approved for public release.

flapping wing at different density ratio, European Journal of Mechanics – B/Fluids Vol. 55, pp. 146–136, 2016.

15. M. Xu, M. Wei, C. Li, and H. Dong, Adjoint-based optimization of flapping plates hinged with a trailing-edge flap, Theoretical and Applied Mechanics Letters, Vol. 5, pp. 1–4, 2015.

16. M. Xu, M. Wei, A continuous adjoint-based approach for the optimization of wing flapping, AIAA paper 2014-2048, Atlanta, GA, 2014.

17. M. Xu, M. Wei, Using adjoint-based approach to study flapping wings, AIAA paper 2013-0839, Grapevine, TX, 2013.

New discoveries, inventions, or patent disclosures:

Do you have any discoveries, inventions, or patent disclosures to report for this period?

No

Please describe and include any notable dates

Do you plan to pursue a claim for personal or organizational intellectual property?

Changes in research objectives (if any):

Change in AFOSR Program Officer, if any:

Extensions granted or milestones slipped, if any:

Extension from May 31, 2015 to May 31, 2016 was granted by AFOSR.

AFOSR LRIR Number

LRIR Title

Reporting Period

Laboratory Task Manager

Program Officer

Research Objectives

Technical Summary

Funding Summary by Cost Category (by FY, \$K)

	Starting FY	FY+1	FY+2
Salary			
Equipment/Facilities			
Supplies			
Total			

Report Document

Report Document - Text Analysis

Report Document - Text Analysis

Appendix Documents

2. Thank You

E-mail user

Aug 26, 2016 14:20:37 Success: Email Sent to: hd6q@virginia.edu